The role of grain boundary mobility in diffusional deformation

Francis Delannay

Université catholique de Louvain, Institute of Mechanics, Materials and Civil Engineering, iMMC/IMAP, Place Sainte Barbe 2, B-1348 Louvain-la-Neuve, Belgium, francis.delannay@uclouvain.be.

Abstract

The model of diffusional deformation is revisited by accounting for the dependence of the diffusion potential on grain boundary curvature. The issue is developed through the analysis of two case-studies: the deformation of a lattice of columnar grains in conditions of Coble creep, and the rotation of a grain embedded in a polycrystal in conditions of either Nabarro-Herring creep or Coble creep. The analysis reveals that, unless grain boundary mobility is infinite, grain boundary curvature is dynamically induced by strain rate. A link is established between the curvature distribution and the transfer of diffusion fluxes across grain boundaries. For the two case-studies, the equation expressing the balance of grain boundary motions at steady-state is solved for calculating, within a range of grain boundary mobilities, the grain boundary profiles, the diffusion fluxes, and the contributions to power dissipation arising from curvature. The latter contributions are found to scale closely as the square of grain size. It follows that the dissipation contribution due to curvature is larger in conditions of Nabarro-Herring creep. In conditions of Coble creep, the dissipation contribution due to curvature translates into a lower bound for the apparent boundary viscosity parameter to be used in numerical simulations. This lower bound is consistent with previous identifications of the parameter in the literature. The classical model assuming flat grain boundaries with transfer of fluxes via triple junctions emerges as a particular case involving the implicit assumption of an infinite grain boundary mobility.

Keywords: grain boundaries (A), diffusion, bulk (A), diffusion, surface (A), creep (A), polycrystalline material (B)

Corresponding author: francis.delannay@uclouvain.be. Tél +32479738784

1. Introduction

"Diffusional deformation" commonly designates the deformation of a polycrystal generated without dislocation activity by diffusion fluxes to and from vacancy sources and sinks located on grain boundaries (GBs). This deformation mode was initially analysed in the pioneering papers of Nabarro, Herring, and Coble (Coble, 1963; Herring, 1950; Nabarro, 1948). The diffusion potential gradients driving diffusion fluxes arise from the fact that the addition/removal of lattice species to/from a GB involves a work proportional to the local traction normal to the GB, T_n (Herring, 1950). The main governing parameters are the average grain size (commonly represented by the radius, R_G, of a cylinder (in 2D) or sphere (in 3D) with volume equal to the average), the diffusion coefficient in the bulk of the grain, D_l, and the product, $D_b\delta$, of the diffusion coefficient in a layer close to the GB times the layer thickness (units in the list of symbols and notations). Bulk diffusion is dominant when $\frac{\delta D_b}{R_G} << D_l$ (Nabarro-Herring creep), and GB-layer diffusion is dominant when $\frac{\delta D_b}{R_G} >> D_l$ (Coble creep). Diffusional deformation is considered to be a major contributor to the rheology during creep under low stress as well as during sintering processes or during the deformation of crystalline rocks in the Earth's mantle. If GBs act as perfect vacancy sources and sinks, strain rate is linear with respect to macroscopic stress (Ashby, 1969). The engineering of superplastic alloys largely exploit the low stress exponent characterising diffusional deformation (Masuda and Sato, 2020). Diffusional deformation may become dominant below a threshold strain rate which decreases with decreasing temperature. At given temperature, the threshold increases when hardening against dislocation activity increases. Diffusional deformation is thus also considered to

contribute to the deformation of nanocrystalline materials close to room temperature when small grain size hinders dislocation activity (Kim et al., 2000; Shah and Chokshi, 1998).

Lifshitz (Lifshitz, 1963) was the first to point out that, as the addition/removal of lattice species to/from the GB brings a velocity difference between adjacent lattices only in the direction normal to the GB, diffusional deformation necessitates a mechanism of sliding bringing a lattice velocity difference, $\Delta\dot{u}_{sl}$, tangent to the GB. Lifshitz proposed to represent the GB as consisting of a thin amorphous layer across which $\Delta\dot{u}_{sl}$ is driven by shear stress tangent to the GB, $T_{//}$, according to the linear law

$$\Delta\dot{u}_{sl} = \frac{1}{\eta} T_{//} . \quad (1)$$

where η results from the mechanisms governing sliding. Although η does not have the conventional units for a viscosity (Pas), Lifshitz proposed to call η the "grain boundary viscosity" (Lifshitz, 1963). According to Lifshitz, $\eta \approx 0$ for a "sufficiently defective" GB but slip may be greatly impeded if the GB is "insufficiently amorphous". Evidence of the occurrence of GB sliding in polycrystals having undergone creep under low-stress or superplastic deformation has been obtained by observation of offsets at the crossing of GBs with fiducial lines drawn on metallographic sections (Bell and Langdon, 1967; Cannon and Sherby, 1977; Fukutomi et al., 1999; Gifkins and Langdon, 1970; Langdon, 1981; Liu and Ma, 2010; Masuda et al., 2019; McNee et al., 2001; McNee et al., 2002; Reynolds et al., 1975; Thorsen and Bilde-Sørensen, 1999). Recently, the GB sliding phenomenon has also been monitored in-situ by high resolution digital image correlation (Linne et al., 2019; Venkataraman et al., 2019). As stated by Ashby (Ashby, 1972), diffusional deformation may thus be regarded either as deformation by diffusional flow of lattice species with GB sliding to accommodate the incompatibilities that

would otherwise appear at GBs, or as deformation by GB sliding with diffusion of lattice species to accommodate the incompatibilities. Yet, two different modes of grain deformation can ensue from this same mechanism: the "Lifshitz" mode observed at small strain, during which grain deformation is close to affine (Delannay and Brassart, 2020; Wei et al., 2008) and the "Rachinger sliding" mode (also quite improperly called "grain boundary sliding (GBS)" mode) observed at large strain, during which deformation proceeds by large relative displacements of grains that remain globally equiaxed (Cannon, 1972; Rachinger, 1952). The conditions governing the transition between these two modes have not been fully elucidated in the literature.

The shear viscosity of a polycrystal, denoted *G*, is the ratio of macroscopic shear-stress to macroscopic shear-strain rate. If the volume-average of the strain rate is identical for all grains, *G* is proportional to the work power per unit volume, $\dot{Q}$, dissipated by the microscopic mechanisms bringing deformation (it follows from variational principles that $\dot{Q}$ is then an upper bound of the effective power dissipation in a random polycrystal (Brassart and Delannay, 2019; Cocks, 1996; Delannay and Brassart, 2020)). According to the diffusional deformation hypotheses, $\dot{Q}$ is the sum of a contribution, $\dot{Q}^{diff}$, due to diffusion fluxes and a contribution, $\dot{Q}^{sl}$, due to GB sliding. While $\dot{Q}^{sl}$ scales as ηR_G, $\dot{Q}^{diff}$ scales either as $\frac{R_G^2}{D_l}$ when bulk diffusion is dominant or as $\frac{R_G^3}{\delta D_b}$ when GB-layer diffusion is dominant (Beere, 1976; Brassart and Delannay, 2019; Delannay and Brassart, 2020; Kim et al., 2004; Lifshitz, 1963; Mori et al., 1997; Mori et al., 1998a; Mori et al., 1998b; Onaka et al., 2001; Riedel et al., 1994). For example, in the case of Coble creep,

$$\frac{\dot{Q}^{sl}}{\dot{Q}^{diff}} \simeq 10\tilde{\eta}_b = 10\frac{\Omega\delta D_b \eta}{kTR_G^2}. \quad (2)$$

where *k* denotes Boltzmann's constant, *T* the absolute temperature, Ω the volume per atom, and $\tilde{\eta}_b$ expresses a non-dimensional GB-viscosity parameter (Delannay and Brassart, 2020; Kim et al., 2004; Riedel et al., 1994). Measurement of the grain size sensitivity exponent of *G* can thus, in principle, reveal whether dissipation is dominated by bulk diffusion, GB-layer diffusion, or GB sliding. The exponent measured experimentally being most frequently close to 2, GB sliding is not considered to be likely to bring a major contribution to dissipation.

At the scale of the crystal lattice, GB sliding is nowadays apprehended in terms of nucleation and glide of disconnections (Han et al., 2018; Hirth, 1994; Hirth and Pond, 1996; Hirth et al., 2016). Accordingly, in a pure polycrystal, the dissipation arising intrinsically from GB sliding is linked to the activation barriers for disconnection nucleation and glide. It was early advocated that this intrinsic dissipation is expected to amount to a negligible fraction of the overall dissipation because the nucleation and glide of disconnections (or GB-dislocations) requires only "shuffling" displacements of lattice constituents in the vicinity of the GB. The length scale of these displacements is much smaller than the length scales of diffusional vacancy transfer between different faces of the grain and/or between the bumps and holes of the undulations created by the ledges and precipitates on the GB (Ashby, 1972; Gibbs, 1965, 1968). According to the analysis of Ashby and co-workers, for a flat, high-angle GB between grains with $R_G \approx 1\mu m$, the intrinsic GB-viscosity arising from shuffling displacements corresponds to $\tilde{\eta}_b^{\text{intrinsic}} \approx 10^{-6}$, whereas, for a serration equivalent to a typical distribution of GB precipitates, the contribution to diffusional transport amounts to $\tilde{\eta}_b \approx 10^{-3}$ (Ashby, 1972; Ashby et al., 1970; Raj and Ashby, 1971). Many authors have thus been prompted to adopt the

approximation of free sliding ($\eta = 0$) (Burton and Greenwood, 1985; Cocks, 1994; Ford et al., 2002; Greenwood, 1985; Greenwood, 1992; Hazzledine and Schneibel, 1993; Pan and Cocks, 1993; Raj and Ashby, 1971; Riedel et al., 1994; Rudge, 2018; Spingarn and Nix, 1978). A few authors have however shown that the free sliding approximation can bring poor agreement between simulations and experimental observations (in particular when deformation is anisotropic), undetermined grain rotation rate, and instability in numerical computations (Beere, 1977; Pan and Cocks, 1993; Wakai and Nikolić, 2011; Wheeler, 2010; Wonisch et al., 2007). This has justified the consideration of values for $\tilde{\eta}_b$ ranging up to 10^{-2} (Wakai and Nikolić, 2011), up to 0.5 (Brassart and Delannay, 2019; Delannay and Brassart, 2020), up to 2 (Henrich et al., 2007), or even up to 10^3 (Kim et al., 2005; Kim et al., 2004; Kim et al., 2009; Wei et al., 2008). Unfortunately, owing to the lack of experimental method giving access at grain scale to the phenomenon of GB sliding, very little data can be found in the literature to validate the value to be ascribed to η. Hence, in numerical models for the simulation of creep, sintering, or Earth's mantle rheology, η is introduced as a phenomenological parameter, which can potentially be identified via a reverse procedure. η then represents an equivalent, apparent GB-viscosity gathering all dissipation phenomena that cannot be ascribed to diffusion fluxes according to the diffusional deformation model.

The present work is motivated by the wish to better apprehend the dissipation contributions that may be hidden behind parameter η. A novel insight is gained by accounting for the dependence of the diffusion potential on GB curvature (Herring, 1953). A non-null curvature implies the parallel occurrence of GB migration (Balluffi et al., 2005). GB mobility then emerges as an additional governing parameter. The analysis reveals that GB curvature is dynamically induced by strain rate. In the literature, the role of GB curvature is at the core of

models for grain growth (Riedel and Svoboda, 1993) whereas the role of pore surface curvature is at the core of models for the first stages of sintering (Delannay and Brassart, 2018; Delannay and Missiaen, 2009; Svoboda and Riedel, 1995a, b). Yet, the models proposed for diffusional deformation did scarcely account for GB curvature. The reason for this neglect is that diffusion fluxes driven by gradients of GB curvature bring no velocity jump between the two adjacent lattices. To our knowledge, the only authors having considered GB curvature are Pan et al. (Ch'ng and Pan, 2004; Pan et al., 1997) who included GB curvature in a finite element formulation of diffusional creep assuming free GB sliding, and Bower and Wininger (Bower and Wininger, 2004) who introduced the full coupling of diffusion and GB sliding with non-zero GB-viscosity in a general finite element scheme for the simulation of the superplastic deformation of columnar polycrystals.

The paper is organized as follows. Section 2 presents the principles of the continuum theory of diffusive GB motion and conservative GB motion assuming isotropic material properties. Based on these principles, two “case-studies” are investigated. Section 3 analyses the small strain deformation of a regular lattice of columnar grains in conditions of Coble creep. Section 4 analyses the steady-state rotation of a particular grain embedded in a columnar polycrystal in conditions of Coble creep or Nabarro-Herring creep. In both Sections, the key equations are established by considering the balance of GB motions and the interactions between GBs and diffusion fluxes. These equations are exploited for calculating GB profiles, diffusion fluxes, and the different contributions to dissipation. In Section 5, the outcomes of the work are evaluated by referring to literature data on GB mobility and GB-viscosity and to microstructural observations.

List of symbols and notations

Subscripts

b	relevant to GB-layer diffusion
e	relevant to external grain with respect to reference grain for GB curvature definition
f	relevant to face labelled *f*
gb	value on the grain boundary
l	relevant to bulk diffusion
n	normal to GB
s	tangent to GB
sl or //	parallel to sliding direction
TJ	relevant to triple junction

Superscripts

X	relevant to point designated by capital letter X
diff	relevant to diffusion fluxes
mig	relevant to GB migration
sl	relevant to grain boundary sliding
T	relevant to diffusion driven by gradient of GB traction
κ	relevant to diffusion driven by gradient of GB curvature

Material properties and physical constants

k	Boltzmann's constant ($J.at^{-1}.K^{-1}$)
D_b	GB-layer diffusion coefficient ($m^2.s^{-1}$)
D_l	bulk diffusion coefficient ($m^2.s^{-1}$)
$\mathcal{D}_b$	GB-layer diffusion parameter $\mathcal{D}_b = \dfrac{\Omega\delta D_b}{kT}$ ($m^5.N^{-1}.s^{-1}$)
$\mathcal{D}_l$	Bulk diffusion parameter $\mathcal{D}_l = \dfrac{\Omega D_l}{k_B T}$ ($m^4.N^{-1}.s^{-1}$)
$\mathcal{M}$	grain boundary mobility ($m^3.N^{-1}.s^{-1}$)
γ	grain boundary tension ($N.m^{-1}$)
δ	thickness of grain boundary diffusion layer (m)
η	apparent grain boundary viscosity ($N.s.m^{-3}$)
$\eta^{\text{intrinsic}}$	intrinsic grain boundary viscosity ($N.s.m^{-3}$)
$\tilde{\eta}_b$, $\tilde{\eta}_l$	non-dimensional GB-viscosity parameters: $\tilde{\eta}_b = \dfrac{\Omega\delta D_b}{kTR_G^2}\eta$, $\tilde{\eta}_l = \dfrac{\Omega D_l}{kTR_G}\eta$ (-)
ψ	dihedral angle (rad)
Ω	volume per atom ($m^3.at^{-1}$)

Scalars and scalar functions

a, a_b, a_l	non-dimensional factors in Eqs. (34), (70), and (76) (-)
h	step height of a grain boundary disconnection (m)
j, j_e	diffusion flux in GB-layer ($m^2.s^{-1}$)
m_b, m_l	non-dimensional parameters defined in Eqs. (35), (71), and (78) (-)
$\dot{u}_n$, $\dot{u}_{ne}$	normal component of the grain boundary velocity with respect to lattice ($m.s^{-1}$)

1	$\Delta\dot{u}_{sl}$	velocity jump at GB between adjacent lattices brought by grain boundary sliding
2		($m.s^{-1}$)
3	$\Delta\dot{u}_{n}$	velocity jump at GB between adjacent lattices in the direction normal to grain
4		boundary ($m.s^{-1}$)
5	x, z	Cartesian coordinates (m)
6	B	half face width of a hexagonal prismatic grain (m)
7	C, C_e	sub-grain centroids (-)
8	$\dot{E}$	principal tensile component of strain rate tensor in pure shear (s^{-1})
9	G	shear viscosity of a polycrystal ($N.m^{-2}.s$)
10	H	distance from grain face to grain centroid (m)
11	M	middle of a grain face (-)
12	P, N	triple junctions (-)
13	O, O_e	centroids of adjacent grains (-)
14	$\dot{Q}$	energy dissipation per unit time and unit volume ($J.s^{-1}.m^{-3}$)
15	R	radial coordinate of a polar system with origin at grain centroid O (m)
16	R_G	radius of cylinder with volume equal to average (m)
17	T	absolute temperature (K)
18	T_n , $T_{//}$	normal and tangent components of grain boundary traction
19	$\mathcal{T}$	torque (N.m)
20	V	volume of grain or portion of grain (m^3)
21	α	orientation of principal tensile axis of strain rate tensor (Fig. 1) (rad)
22	φ	slope of GB profile (-)
23	κ, κ_e	grain boundary curvature (m^{-1})
24	μ	diffusion potential ($J.at^{-1}$)
25	μ_{atom}, μ_V	chemical potential of atom and vacancy ($J.at^{-1}$)
26	ν	coordinate along normal vector **n** defined positive outward with respect to
27		reference grain (m)
28	θ	azimuthal coordinate of a polar system with origin at grain centroid O (rad)
29	$\dot{\theta}$	angular grain rotation velocity ($rads^{-1}$)
30		
31	*Vectors, tensors, and matrices*	
32	**b**	Burgers vector of a grain boundary disconnection (m)
33	$\dot{\mathbf{E}}$	macroscopic strain rate tensor (s^{-1})
34	**J**, $\mathbf{J}_e$	diffusion flux in the bulk of the grain ($m.s^{-1}$)
35	**n, s**	unit vectors normal and tangent to grain boundary (m)
36	**U**	position vector (m)
37	$\dot{\mathbf{U}}$	velocity of a material point inside the grain ($m.s^{-1}$)
38	$\Delta\dot{\mathbf{u}}$	velocity jump between adjacent lattices at GB ($m.s^{-1}$)
39	**T**	traction on grain boundary ($N.m^{-2}$)
40	**x**, **z**	unit vectors of a Cartesian coordinate with origin at grain face centroid M and **z**
41		oriented in direction of vector $\overrightarrow{OO_e}$ (m)
42	$\boldsymbol{\sigma}$	local stress tensor ($N.m^{-2}$)

2. Diffusive and conservative grain boundary motions.

Before introducing the theoretical basics at the continuum scale, we first outline the phenomena at the crystal scale.

2.1. Physics at the microscale

Figure 1 represents the cross-section of three columnar grains, labelled A, B, and C, sharing a common TJ. The grains are taken to be identical mono-component phases differing only by the orientation of the lattice. White squares depict vacancies. Geometrically, GBs are two-dimensional entities of which the crystallography is characterised by five degrees of freedom. At crystal scale, the GB consists in a succession of terraces containing plateaus and steps: the continuous lines in Fig. 1 represent the three GBs at a scale at which the concept of GB curvature can apply. In the present work, crystalline anisotropy is neglected and all material properties are assumed isotropic. The three dihedral angles at TJs will be supposed to always keep the isotropic equilibrium value $\psi = \frac{2\pi}{3}$. GBs contain a distribution of linear defects which, today, are apprehended via the concept of "disconnections" (Hirth, 1994; Hirth and Pond, 1996) (details on the role of disconnections in GB kinetics can be found in the recent review of Han et al (Han et al., 2018)). Disconnections have a mixed character: they combine a dislocation character defined by a Burgers vector and a step character defined by a step height. Disconnections having the same Burgers vector can differ by step height, and conversely. A general disconnection can dissociate into sessile disconnections having Burgers vector perpendicular to the GB (depicted in red in Fig. 1) and glissile disconnections having Burgers vector parallel to the GB (depicted in green).

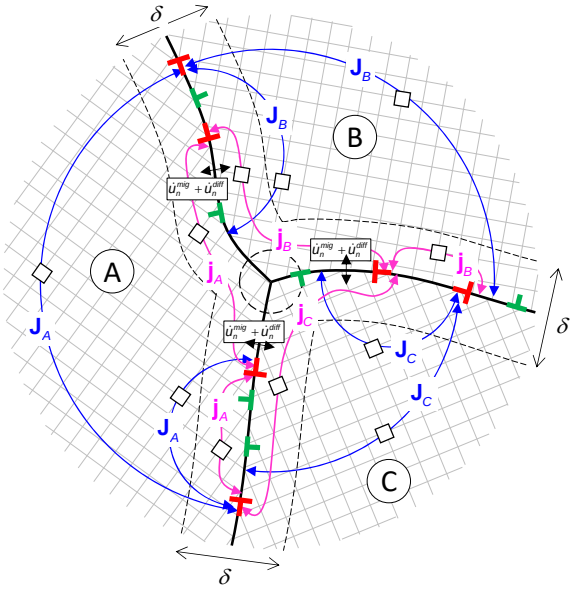

Figure 1: Cross-section of three columnar grains sharing a common TJ. Disconnections having Burgers vector perpendicular and parallel to GB are depicted in red and green, respectively. green). Blue arrows denoted **J** represent diffusion fluxes flowing through the bulk of the grain. Magenta arrows denoted **j** represent diffusion fluxes inside GB-layers of thickness δ. Black arrows represent total GB motion velocity $\dot{u}_n^{diff} + \dot{u}_n^{mig}$.

Diffusion fluxes in the bulk of the grain, denoted **J** (blue arrows in Fig. 1), are defined as volumes of atoms (or lattice components) transported per unit surface and per unit time. They are driven by the gradient of the diffusion potential, denoted $\mu = \mu_{atom} - \mu_V$ where μ_{atom} and μ_V denote the chemical potential of atom (or lattice component) and of vacancy, as (Balluffi et al., 2005; Herring, 1950)

$$\mathbf{J} = -\frac{D_l}{kT}\nabla\left(\mu_{atom} - \mu_V\right) = -\frac{D_l}{kT}\nabla\mu = -\frac{\mathcal{D}_l}{\Omega}\nabla\mu \tag{3}$$

$\frac{\mathcal{D}_l}{\Omega} = \frac{D_l}{kT}$ is the Onsager diffusion coefficient. In a mono-component polycrystal, gradients of μ arise from the presence of vacancy sources and sinks. The Nabarro-Herring-Coble model

assumes that the vacancy sources and sinks are located only on GBs, which implies that the divergence of $\mathbf{J}$ is null in the grain interior, i.e. density is uniform and μ is harmonic. The vacancy sources and sinks are the cores of disconnections having a Burgers vector perpendicular to the GB (depicted in red in Fig.1), which can be brought to climb along the GB by absorbing or emitting a vacancy. We consider in the present work that this mechanism is "perfect", i.e. we assume the absence of activation barrier for the capture/emission of vacancies by the core of climbing disconnections. Equilibrium vacancy concentration is thus assumed to always be maintained at GBs.

Owing to the internal stress field arising from disconnections and other sources of lattice distortion, the diffusion coefficient is larger close to the GB than in the bulk of the grains. This is commonly modelled by assuming the existence of a GB-layer of thickness δ (Fig. 1) inside which the average diffusion coefficient, D_b, is larger than the diffusion coefficient D_l in the bulk (Fisher, 1951). As D_b depends on δ, only the product δD_b is a meaningful material property: a frequent assumption is $\delta \approx 1$ nm (Herzig and Mishin, 2005). Vacancies travel from sources to sinks via either of the two lattices (Balluffi, 1982). Like for bulk diffusion fluxes, we may thus distinguish two fluxes flowing along half-layers of thickness $\frac{\delta}{2}$ separated by the GB (magenta arrows in Fig. 1). These fluxes, denoted ***j*****,** are parallel the GB and are defined in units of volume per unit length and per unit time. The distinction between two fluxes makes possible an account for the effect of a potential difference between the two sides. As δ is small, μ inside the GB-layer is very close to the diffusion potential on the GB, denoted μ_{gb}, and, based on Eq. (3),

$$j = J_{//\delta/2}\frac{\delta}{2} = -\frac{1}{2}\frac{\delta D_b}{kT}\nabla_s \mu_{gb} = -\frac{1}{2}\frac{\mathcal{D}_b}{\Omega}\nabla_s \mu_{gb} \qquad (4)$$

where $J_{//\delta/2}$ is the bulk flux component parallel to the GB inside the half layer, ∇_s denotes the gradient operator on the GB surface, and $\mathcal{D}_b = \frac{\Omega\delta D_b}{kT}$ ($\mathcal{D}_l$ and $\mathcal{D}_b$ have thus different units). Both types of diffusion fluxes, **J** and *j*, can transport matter between different grain faces or between different points on the same face. A priori, neither **J** nor *j* are identical on the two sides of the GB.

By definition, GB motion designates the displacement of a GB with respect to a crystal lattice. The motion of disconnections brings a displacement of the GB with respect to the two adjacent lattices together with a displacement of the two lattices with respect to one another (except when disconnections have a pure step character, i.e. when the Burgers vector is null). Three types of GB velocity can be distinguished, which we call "diffusive GB velocity", "GB sliding velocity", and "GB migration velocity".

(i) The climbing of a disconnection with Burgers vector perpendicular to the GB brings the addition/subtraction of one lattice plane in one or the other of the two adjacent lattices. This amounts to a normal displacement of the GB with respect the lattice. We denote $\dot{u}_{nA}^{diff}$ the displacement velocity of the GB with respect to lattice A on one side of the GB. The superscript "diff" reminds that this type of GB motion results from diffusional transport. $\dot{u}_{nA}^{diff}$ is the volume of matter per unit surface and per unit time that deposits onto, or leaves from, a particular point on the side A of the GB. The normal velocity jump between the two lattices at the GB, denoted $\Delta\dot{u}_n$, is the sum of the two contributions: $\Delta\dot{u}_n = \dot{u}_{nA}^{diff} + \dot{u}_{nB}^{diff}$. In the literature, $\dot{u}_n^{diff}$ is sometimes called "diffusive GB migration": we call it "diffusive GB velocity" because it is important to not to confuse $\dot{u}_n^{diff}$ with the GB velocity arising from the migration phenomenon.

(ii) As introduced already in Section 1, the GB sliding velocity, $\Delta\dot{u}_{sl}$, i.e. the tangent velocity jump at the GB, results from the glide of disconnections having a Burgers vector parallel to the GB (depicted in green in Fig.1). In contrast to climb, disconnection glide requires only small-range shuffling displacements of the lattice constituents on the two sides of the GB, without contribution of long-range diffusion. For this reason, GB sliding is qualified as conservative GB motion (Balluffi et al., 2005). The Burgers vector of the gliding disconnections defines the GB sliding direction whereas the step height multiplied by the disconnection density defines the direction of the GB with respect to the sliding direction. If grain rigidity is infinite, the sliding direction as well as the sliding velocity are uniform on the GB. This means that, in the case of a curved GB, the sliding direction is not locally tangent to the GB.

(iii) The displacement of a step along the GB amounts to the direct transfer of a lattice constituent from one grain to the adjacent grain. This mode of GB motion, which is also conservative, is called GB migration. The GB migration velocity will be denoted $\dot{u}_n^{mig}$. The total normal velocity of the GB (depicted by black arrows in Fig. 1) is thus $\dot{u}_n^{diff} + \dot{u}_n^{mig}$. In contrast to $\dot{u}_n^{diff}$, $\dot{u}_n^{mig}$ does not amount to a drift velocity of the material points on the GB. The GB migration velocities being opposite with respect to the two lattices, GB migration does not contribute to a normal velocity jump $\Delta\dot{u}_n$ at the GB.

Owing to the mixed character of a disconnection, the climb of a sessile disconnection or the glide of a glissile disconnection both involves the displacement of a step, i.e. they bring about concomitantly GB migration. In particular, when both $\dot{u}_n^{mig} \neq 0$ and $\Delta\dot{u}_{sl} \neq 0$, GB motion is said to be “shear-coupled” (Cahn et al., 2006; Cahn and Taylor, 2004). Pure GB sliding (

$\Delta\dot{u}_{sl} \neq 0$, $\dot{u}_n^{mig} = 0$) and pure GB migration ($\Delta\dot{u}_{sl} = 0$, $\dot{u}_n^{mig} \neq 0$) can be apprehended as resulting from the motion of a collection of disconnections having the same Burgers vector with different (positive and negative) step heights, and conversely. Simulations based on molecular dynamics indicate that the shear coupling effect tends to vanish when temperature increases above 0.5 T_m (Cahn et al., 2006). The continuum theory of GB motion assuming isotropic material properties can deal only with the phenomena of pure GB sliding and pure GB migration.

2.2. Continuum theory

At the continuum scale, it is possible to define the traction vector on the GB, **T**, and the curvature of the GB, κ. **T** and κ are independent quantities. Vector **T** (with units of force per unit surface) at a particular point can be derived from the local stress, σ_{ij}, via Cauchy's law:

$$T_i = \sigma_{ij} n_j \tag{5}$$

where **n** denotes a unit vector normal to the GB and summation over repeated indices is implied. The local stress is the sum of two contributions: the stress due to the load remotely applied on the polycrystal and the internal stresses due to the population of crystal defects (i.e. disconnections). The continuum scale is assumed to be large enough for considering that internal stresses arise from a continuous distribution of defects rather than from isolated singular defects. The (mean) curvature, κ, at a point is defined by reference to one of the two adjacent grains:

$$\kappa = \frac{1}{\rho_1} + \frac{1}{\rho_2} \tag{6}$$

where ρ_1 and ρ_2 are the local principal radii of curvature, which are defined positive or negative when the reference grain is, respectively, convex or concave. Curvature is thus opposite on the

two sides of the GB. At the microscale, GB curvature is generated by a gradient of the product of the disconnection density times the average disconnection step height. In order to account for the change of sign of κ, subscript *e* is used in the following when designating a quantity pertaining to the grain on the external side of the GB with respect to the reference grain. The absence of subscript *e* thus denotes a quantity pertaining to the internal side: for example, we write $\kappa_e = -\kappa$.

In the presence of T_n and κ, the absorption/desorption of vacancies at sinks/sources on the GB generates a work. It follows that the diffusion potential, μ, is affected by both T_n and κ. On the GB, μ_{gb} expresses differently on the two sides (Herring, 1950, 1953):

$$\mu_{gb} - \mu^\circ = \mu_{gb}^T + \mu_{gb}^\kappa = -\Omega T_n + \Omega\gamma\kappa \quad (7)$$

and $$\mu_{gbe} - \mu^\circ = \mu_{gb}^T + \mu_{gbe}^\kappa = -\Omega T_n - \Omega\gamma\kappa \quad (8)$$

(μ° is a reference potential that may be taken null without loss of generality and subscript gb designates a value on the GB). There is thus a change of diffusion potential $\Delta\mu = -2\Omega\gamma\kappa$ when a curved GB is crossed from the internal side to the external side. This change operates across a thickness of a few unit cells inside which the distortion of chemical bonds gives rise to the GB excess energy. This thickness size plays no role in continuum models as long as it is much smaller than grain size.

Being quantities defined for a continuous medium, T_n and κ lose meaning at small distances from a triple junction (TJ) (just like stress field loses meaning inside a dislocation core). The size of the TJ core inside which T_n and κ cannot be defined (depicted by a dashed circle in Fig 1) amounts to a few unit cells. Like GB thickness, the TJ core size plays no role in continuum models as long as it is much smaller than the grain size. Eqs. (7) and (8) do thus not

apply inside the TJ core. Otherwise, continuity of μ would require (i) that, at any TJ, T_n should be identical for the three GBs (this may be postulated only if the activation barrier for the nucleation of disconnections at TJs is neglected), and (ii) that GB curvature should always tend to zero at TJs. Scrutiny must thus be exercised for the interpretation of the tendencies close to TJs of the results derived from the continuum theory.

At zero strain rate, the thermodynamic equilibrium of a polycrystal without porosity implies the uniformity of the sum $T_n + \gamma\kappa$ within the whole GB network. This condition cannot be achieved in the presence of GB curvature because the field of tractions T_n needed to compensate for the non-uniformity of GB curvature would not be equilibrated. Thermodynamic equilibrium at zero strain rate would thus imply flat GBs together with a purely hydrostatic macroscopic stress. If the macroscopic stress has a deviatoric component, the T_n field on GBs is not uniform, which, in the presence of vacancy sources and sinks, brings about a field of diffusion potential gradient driving diffusional transport from GB to GB.

Diffusive GB velocities, $\dot{u}_n^{diff}$ and $\dot{u}_{ne}^{diff}$, are the sum of two contributions: the normal component of bulk fluxes **J** and $\mathbf{J}_e$, and the opposite of the divergence (in the GB plane) of GB-layer fluxes j and j_e. $\dot{u}_n^{diff}$ and $\dot{u}_{ne}^{diff}$ can moreover be decomposed into contributions due to T_n and to κ: $\dot{u}_n^{diff} = \dot{u}_n^T + \dot{u}_n^\kappa$; $\dot{u}_{ne}^{diff} = \dot{u}_{ne}^T + \dot{u}_{ne}^\kappa$ (use is made in the following of superscript T for denoting a quantity that is a function of the normal traction component T_n and superscript κ for a quantity that is a function of GB curvature). Denoting ν the coordinate in the direction of the normal vector **n** defined positive outward from the reference grain, these contributions write, according to Eqs. (3), (4) (7), and (8),

$$\dot{u}_n^T = -\frac{\mathcal{D}_l}{\Omega}\left(\frac{\partial \mu^T}{\partial \nu}\right)_{gb} - \frac{1}{2}\mathcal{D}_b \nabla_s^2 T_n \,. \tag{9}$$

$$\dot{u}_{ne}^T = \frac{\mathcal{D}_l}{\Omega}\left(\frac{\partial \mu^T}{\partial \nu}\right)_{gbe} - \frac{1}{2}\mathcal{D}_b \nabla_s^2 T_n \tag{10}$$

$$\dot{u}_n^\kappa = -\frac{\mathcal{D}_l}{\Omega}\left(\frac{\partial \mu^\kappa}{\partial \nu}\right)_{gb} + \frac{1}{2}\mathcal{D}_b \nabla_s^2 \left(\gamma\kappa\right). \tag{11}$$

and $$\dot{u}_{ne}^\kappa = \frac{\mathcal{D}_l}{\Omega}\left(\frac{\partial \mu^\kappa}{\partial \nu}\right)_{gbe} - \frac{1}{2}\mathcal{D}_b \nabla_s^2 \left(\gamma\kappa\right) \tag{12}$$

Eqs (9) to (12) imply that $\dot{u}_n^{diff}$ is positive if oriented along the outgoing normal with respect to the internal grain whereas $\dot{u}_{ne}^{diff}$ is positive if oriented along the outgoing normal with respect to the external grain. The first term on the rhs may be neglected with respect to the second term in conditions of Coble creep ($R_G << \frac{\delta D_b}{D_l}$), and reversely in conditions of Nabarro-Herring creep, ($R_G >> \frac{\delta D_b}{D_l}$) (Raj and Ashby, 1971). At the temperature relevant for creep or for sintering, the characteristic length $\frac{\delta D_b}{D_l}$ is commonly considered to be of the order of 1 μm. In the following, quantities valid only under either of the two conditions of diffusion dominance will be designated by subscripts b and l, respectively.

It results from Eqs. (4), (7), and (8) that $j^T = j_e^T$ whereas $j^\kappa = -j_e^\kappa$. As a consequence, the two GB-layers of thickness $\frac{\delta}{2}$ may, in the absence of curvature, be considered as a single layer of thickness δ in which the diffusion flux is $j = j^T + j_e^T$. The emission or absorption of

vacancies on the GB affects μ in the same way on the two sides of the GB. The gradients $\frac{\partial \mu^T}{\partial v}$ in the vicinity of a flat GB are thus opposite:

$$\left(\frac{\partial \mu^T}{\partial v}\right)_{gb} = -\left(\frac{\partial \mu^T}{\partial v}\right)_{gbe}, \tag{13}$$

and, it follows from to Eqs. (9) and (10) that

$$\dot{u}_{ne}^T = \dot{u}_n^T . \tag{14}$$

In contrast, GB curvature affects μ in opposite ways on the two sides, hence

$$\left(\frac{\partial \mu^\kappa}{\partial v}\right)_{gb} = \left(\frac{\partial \mu^\kappa}{\partial v}\right)_{gbe} . \tag{15}$$

and $$\dot{u}_{ne}^\kappa = -\dot{u}_n^\kappa . \tag{16}$$

Diffusion driven by GB curvature does thus not generate a normal velocity jump at the GB: $\Delta \dot{u}_n^\kappa = \dot{u}_{ne}^\kappa + \dot{u}_n^\kappa = 0$.

The driving force for GB migration is the difference of chemical potential of the atom, μ_{atom}, in the lattices on the two sides of the GB. In the case of isotropic grains of the same phase without internal stresses, $\mu_{atom_e} - \mu_{atom} = -\Omega\gamma\kappa$. The migration velocity, $\dot{u}_n^{mig}$, is commonly expressed in the form

$$\dot{u}_n^{mig} = -\dot{u}_{ne}^{mig} = \mathcal{M}\frac{\mu_{atom_e} - \mu_{atom}}{\Omega} = -\mathcal{M}\gamma\kappa \tag{17}$$

where $\mathcal{M}$ is the GB mobility (the same convention of sign applies as for $\dot{u}_n^{diff}$ and $\dot{u}_{ne}^{diff}$). If negative, $\dot{u}_n^{mig}$ represents the velocity of transfer of lattice components across the GB from the interior side to the exterior side. Hence, Eq. (17) implies that no transfer of matter across a GB can occur without GB curvature. Owing to the fact that they both have equal and opposite

values on the two sides of the GB, it is tempting to assimilate $\dot{u}_n^{mig}$ and $\dot{u}_n^{\kappa}$. The fundamental difference between these two types of GB velocity (which is attested by their different dependence on κ in Eqs. (11), (12) and (17)) is a key feature in the context of the present work.

$\mathcal{M}$ is the isotropic GB mobility under zero shear traction, which can be characterized via measurement of grain growth rate during heat-treatment. Comparison of Eqs. (17) and (1) shows that $\mathcal{M}$ and η^{-1} have the same units. Like $\eta^{\text{intrinsic}}$, $\mathcal{M}$ is the average of the intrinsic resistance to conservative GB motion which depends on the local GB crystallography. $\mathcal{M}$ does thus not depend on grain size and microstructure. In contrast, as mentioned in Section 1, parameter η may, in the practice, represent an apparent GB-viscosity involving, in addition to $\eta^{\text{intrinsic}}$, the effect of dissipation phenomena that cannot be ascribed to diffusion fluxes.

3. Deformation of a regular lattice of columnar grains

3.1. The classical model

In the following, vector $\mathbf{U}$ denotes the position of a material point and vector $\dot{\mathbf{U}}$ the velocity of the point (whereas, as mentioned in Section 2, $\dot{\mathbf{u}}$ denotes the GB velocity with respect to the lattice and $\Delta\dot{\mathbf{u}}$ the lattice velocity jump at the GB). In the case of the diffusional deformation mode, the deformation of a polycrystal may be said to be affine if grains do not rotate with respect to one another while the velocity difference $\dot{\mathbf{U}}^{O'} - \dot{\mathbf{U}}^{O}$ between the material points located at centroids O and O' of two grains remains linked to the macroscopic strain rate tensor $\dot{\mathbf{E}}$ via

$$\dot{U}_i^{O'} - \dot{U}_i^{O} = \dot{E}_{ij} R_j^{O} \tag{18}$$

where $\mathbf{R}^O$ denotes vector $\overrightarrow{OO'}$. The deformation of a periodic lattice of grains is affine by definition. In the case of a random polycrystal, it follows from variational principles that the hypothesis of affine deformation brings only an upper bound for the power dissipated during deformation. This upper bound is nevertheless realistic because, within the limits of small deformation, the departure from periodicity does not bring the average velocity field to differ very much from the affine approximation (Delannay and Brassart, 2020). The affine hypothesis does not apply for the Rachinger mode of deformation which proceeds by large relative displacements of grains that remain globally equiaxed. If grain rotation is null, $\dot{\mathbf{U}}^{O'} - \dot{\mathbf{U}}^{O} = \Delta\dot{\mathbf{u}}$. During diffusional deformation, the component of $\Delta\dot{\mathbf{u}}$ normal to GB, $\Delta\dot{u}_n$, is driven by the gradients of μ^T arising from the dependence of T_n on GB orientation, whereas the tangent component is the GB sliding velocity, $\Delta\dot{u}_{sl}$, driven by $T_{//}$ according to Eq. (1).

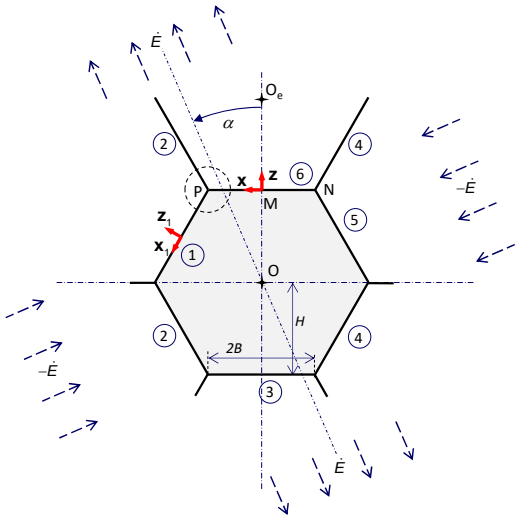

Figure 2: Geometrical parameters for the analysis of the affine deformation of a lattice of hexagonal grains

Although the analysis could apply as well to a 3D polycrystal, we limit ourselves to a columnar polycrystal. As only three GBs meet at each TJ, the grains are polygonal prisms

having six faces on average. If grains are equiaxed, the representative grain at zero strain rate is a regular hexagonal prism with flat faces. The effect of the GB curvature (which drives grain growth in a random polycrystal at rest) is thus ignored. As represented in Figure 2, we consider a purely deviatoric macroscopic strain rate with principal tensile direction, of amplitude $\dot{E}$, oriented along an angle α with respect to the normal to one of the grain faces. *H* is the initial distance from grain centroid to GB middle. As we limit the analysis to small deformation, this distance will be approximated as remaining equal to *H*. The distance between the two TJs at the ends of a GB is denoted $2B = 2\frac{H}{\sqrt{3}}$. In the following, *B* will be used as reference length, which can be converted into the radius of the equivalent cylinder via

$$R_G = \sqrt{\frac{6\sqrt{3}}{\pi}}B = 1.82\,B \tag{19}$$

Letter O designates the centroid of the grain used as reference for the definition of κ whereas O_e designates the centroid of an adjacent grain. Faces are designated by subscript $1 \le f \le 6$, which are taken to increase anticlockwise, with faces *f* = 3 and *f* = 6 horizontal. For each face, a Cartesian coordinate system with origin at GB middle is defined by unit vectors **x** and **z**, with **z** oriented in direction $\overrightarrow{OO_e}$ and **x** defined positive anticlockwise with respect to O. Whatever the GB shape during straining, the direction of GB sliding (i.e. the direction of the Burgers vector of the GB disconnections of which glide is activated) is thus parallel to **x**. This also means $T_{//} \equiv T_x$ (Eq. (1)). Via Eq.(18), the components of the velocity jumps at the six GBs express

$$\left(\Delta\dot{u}_z\right)_f \equiv \left(\Delta\dot{u}_n\right)_f = 2\sqrt{3}B\dot{E}\cos\left(2\alpha - 2f\frac{\pi}{3}\right) \tag{20}$$

$$\left(\Delta\dot{u}_x\right)_f \equiv \left(\Delta\dot{u}_{sl}\right)_f = 2\sqrt{3}B\dot{E}\sin\left(2\alpha - 2f\frac{\pi}{3}\right) \tag{21}$$

The middle of the horizontal GB labelled $f = 6$ is designated by letter M whereas the two TJs at the ends are designated by letters P and N, for x positive and negative, respectively.

In the literature, it has always been assumed that, during diffusional deformation, GBs remain flat and parallel to their direction at zero strain (we will show in section 3.2 that the flat GB is only one of the possible GB shapes). Based on this assumption, several authors have calculated the shear viscosity of a regular lattice of hexagonal prismatic grains: Spingarn and Nix for Coble creep with free sliding ($\eta = 0$) (Spingarn and Nix, 1978); Kim et al for Coble creep with $\eta \neq 0$ (Kim et al., 2004); Rudge (Rudge, 2018) for Nabarro-Herring creep with $\eta = 0$. The distribution of T_n along GBs is parabolic and, if the activation barrier for the nucleation of disconnections at TJs is neglected, $T_n = 0$ at TJs. In the following, the novel features that emerge when GB curvature is accounted for will be highlighted without reiterating the developments for flat GBs: the latter keep holding and can be found in the literature.

3.2. GB curvature and transfer of diffusion fluxes across GBs during quasi-steady-state deformation

When a polycrystal is deformed under strain rate control, the application of the macroscopic strain rate initiates a transient stage followed by a stage of quasi-steady-state. During the transient stage, a curvature distribution grows progressively along the GBs while the relative velocity of the TJs evolves consistently with the constraint that the equilibrium dihedral angle $\psi = \frac{2\pi}{3}$ be always maintained. During the stage of quasi-steady-state, the curvature distribution along the GBs remains homothetical while the relative velocities of TJs comply with Eq. (18). This means that, during quasi-steady state, the component $\dot{u}_n^T$ of the diffusional GB velocity (Eqs. (9)and (10)) brings the evolution of the relative GB sizes according to strain rate

while the coupling of the component $\dot{u}_n^{\kappa}$ with the migration velocity $\dot{u}_n^{mig}$ (Eqs (11), (12), and (17)) brings the GB shapes to remain stationary. Stationarity of GB shapes implies that the resultant of $\dot{u}_n^{\kappa}$ and $\dot{u}_n^{mig}$ is null during quasi-steady-state:

$$\dot{u}_n^{\kappa} + \dot{u}_n^{mig} = 0 , \tag{22}$$

i.e., via Eqs. (11) and (17),

$$\frac{\mathcal{D}_l}{\Omega}\left(\frac{\partial \mu^{\kappa}}{\partial \nu}\right)_{gb} - \frac{1}{2}\mathcal{D}_b \nabla_s^2\left(\gamma\kappa\right) + \mathcal{M}\gamma\kappa = 0 \tag{23}$$

Eq. (23) establishes a link between diffusivities $\mathcal{D}_l$ and $\mathcal{D}_b$ and GB mobility $\mathcal{M}$ during quasi-steady-state. We assume that the strain rate is small enough for allowing the validity of the small strain approximation to apply when the quasi-steady-state is reached. Eq. (22) means that any volume of matter $\dot{u}_n^{\kappa}$ or $\dot{u}_{ne}^{\kappa}$ that deposits on one side of the GB is, via GB migration, transferred to the other side from which it diffuses away owing to the opposite sign of the divergence of the curvature gradient. The transfer of diffusion fluxes across GBs is thus triggered by the presence of curvature.

The GBs across which diffusion fluxes are transferred are the GBs along which sliding occurs. Before developing the mathematics, we illustrate this feature by depicting in Figure 3 an enlarged view of the area around the TJ denoted P in Fig. 2 (area circumscribed by a dotted circle in Fig. 2). The curvature of the GBs is not drawn: the actual GB profiles during straining will be represented in Figs. 7a and 7b. Assuming the conditions of Coble creep, the trajectories of the atom fluxes in the GB-layers (magenta arrows denoted **j**) are sketched for two orientations of loading: $\alpha = 0$ and $\alpha = -\frac{\pi}{4}$ (similar trajectories could be drawn for bulk fluxes in conditions of Nabarro-Herring creep). When $\alpha = 0$, identical fluxes are emitted on the two

sides of GBs *f* = 1 and *f* = 2 whereas identical fluxes adsorb on the two side of GB *f* = 6. This process brings some of the flux trajectories to cross GBs *f* = 1 and *f* = 2, for which $\Delta\dot{u}_{sl} \neq 0$, whereas no flux crosses GB *f* = 6, for which $\Delta\dot{u}_{sl} = 0$. The trajectories drawn in Fig. 3a will be justified in Fig. 8b. When $\alpha = -\frac{\pi}{4}$, GB *f* = 6 is under pure shear, identical fluxes are emitted on the two sides of GB *f* = 1, and identical fluxes are adsorbed on the two side of GB *f* = 2. In that case, $\Delta\dot{u}_{sl} \neq 0$ for all three GBs, which are all crossed by some flux trajectories.

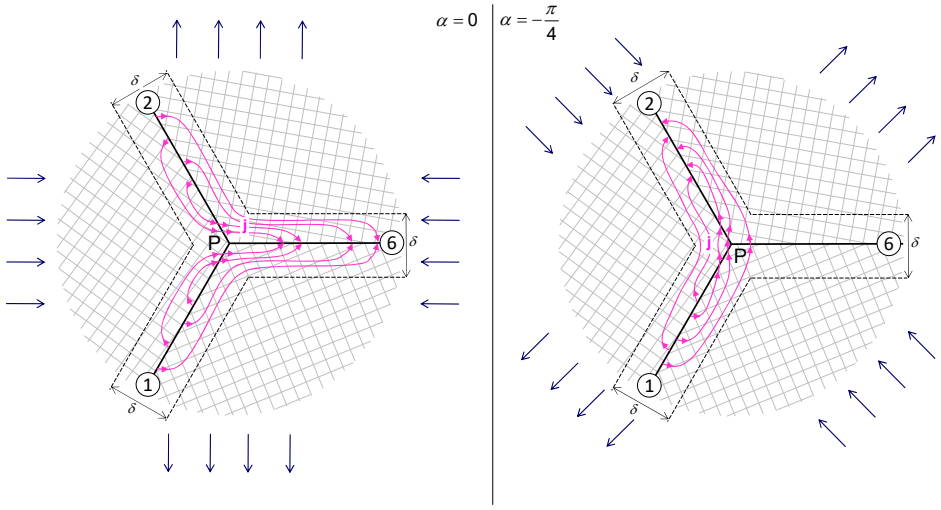

Figure 3: Enlarged view of the area around the TJ denoted P in Fig. 2: the trajectories of the atom fluxes in the GB-layers (magenta arrows denoted **j**) are sketched for loading orientations

$$\alpha = 0 \text{ and } \alpha = -\frac{\pi}{4}$$

Let us consider, as represented in Figure 4, the cross-section of two triangular grain portions with apexes at O, P, and N and O_e, N, and P, which are submitted to an arbitrary strain rate, i.e. an arbitrary velocity jump $\Delta\dot{\mathbf{u}} = \left(\Delta\dot{u}_{sl}, \Delta\dot{u}_n\right)$ at GB PN. If adjacent grains have the same size, the GB profiles under straining present central symmetry with respect to GB middle, i.e. $\kappa(s)$ is an odd function of *s,* hence also $\dot{u}_n^{\kappa}(s)$ and $\dot{u}_n^{mig}(s)$. The six GB profiles moreover

present central symmetry with respect to grain centroid. The centroids of the grain portions OPN and O_eNP are denoted by letters C and C_e. The link between GB curvature and the flow of matter across the GB can be established by considering the components $\dot{U}_x^C$ and $\dot{U}_x^{C_e}$ of the velocity of C and C_e.

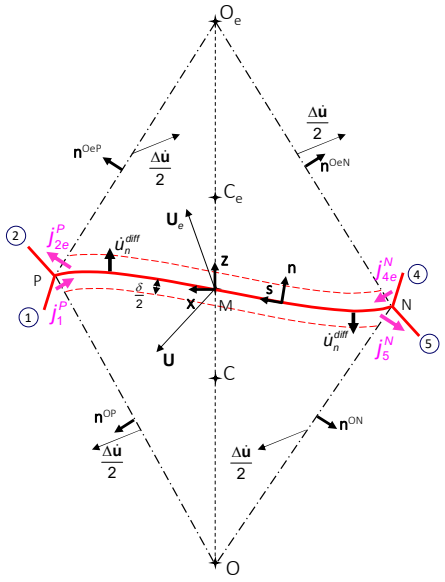

Figure 4. Parameters for the calculation the velocity of the centroids of adjacent sub-grains

Via the divergence theorem, the velocity, $\dot{\mathbf{U}}^C$, of the centroid of a body of non-compressible matter with uniform density can be expressed as (Wakai and Brakke, 2011)

$$\dot{U}_i^C = \frac{1}{V}\int_V \dot{U}_i dV = \frac{1}{V}\int_V \nabla\cdot\left(U_i\dot{\mathbf{U}}\right)dV = \frac{1}{V}\int_S U_i\left(\dot{\mathbf{U}}\cdot\mathbf{n}\right)dS \qquad (24)$$

where *V* denotes the body volume and *dS* denotes a surface increment. We take the origin at point M (Fig. 4) and, as represented in Fig. 4, we assume the conditions of Coble creep (Nabarro-Herring conditions will be analysed in Section 4). For the centroid of sub-grain OPN, $\dot{U}_x^C = -\frac{\Delta\dot{u}_{sl}}{2}$. On faces OP and ON, $\left(\dot{\mathbf{U}}\cdot\mathbf{n}^{OP}\right) = \frac{\Delta\dot{\mathbf{u}}}{2}\cdot\mathbf{n}^{OP} = -\frac{\sqrt{3}}{2}\frac{\Delta\dot{u}_{sl}}{2} - \frac{1}{2}\frac{\Delta\dot{u}_n}{2}$ and

$\left(\dot{\mathbf{U}}\cdot\mathbf{n}^{ON}\right)=\frac{\Delta\dot{\mathbf{u}}}{2}\cdot\mathbf{n}^{ON}=\frac{\sqrt{3}}{2}\frac{\Delta\dot{u}_{sl}}{2}-\frac{1}{2}\frac{\Delta\dot{u}_{n}}{2}$. The sum of the terms of integration along OP and ON thus yields $-\frac{\Delta\dot{u}_{sl}}{2}$, which is equal to $\dot{U}_x^C$. This implies that the sum of the terms of integration along the GB and across the two GB-layers of thickness $\delta/2$ is null. Along the GB, $\left(\dot{\mathbf{U}}\cdot\mathbf{n}\right)=\dot{u}_n^{diff}$ (migration velocity $\dot{u}_n^{mig}$ does not represent a velocity of matter) whereas, across the diffusion layers, $\int_{gbl}U_x\left(\dot{\mathbf{U}}\cdot\mathbf{n}\right)ds\cong Bj$. Hence, denoting j_1^P the diffusion flux at P that flows to/from the GB-layer f = 1 (Figure 4), may be approximated as

$$B\left(j_1^P+j_5^N\right)=-\int_{GB}x\dot{u}_n^{diff}ds=-\int_{GB}x\left(\dot{u}_n^T+\dot{u}_n^\kappa\right)ds\,. \tag{25}$$

Eq. (25) does not depend on the geometry of the grain portion bounded by GB PN on which Eq. (24) is applied. j_1^P and j_5^N are the sum of flux contributions arising from GB tractions and from GB curvature: $j_1^P=j_1^{TP}+j_1^{\kappa P}$; $j_5^N=j_5^{TN}+j_5^{\kappa N}$. As symmetry imposes that $j^T=0$ at GB middle, j_1^P and j_5^N can, based on Eqs (20) and (21), be expressed in terms of $\Delta\dot{u}_n$ and $\Delta\dot{u}_{sl}$ as

$$j_1^P=\frac{B}{4}\left(-\Delta\dot{u}_n+\sqrt{3}\Delta\dot{u}_{sl}\right)+j_1^{\kappa P} \tag{26}$$

$$j_5^N=\frac{B}{4}\left(\Delta\dot{u}_n+\sqrt{3}\Delta\dot{u}_{sl}\right)+j_5^{\kappa N} \tag{27}$$

Eq. (25) thus translates into

$$\frac{\sqrt{3}}{2}B^2\Delta\dot{u}_{sl}+B\left(j_1^{\kappa P}+j_5^{\kappa N}\right)=-\int_{GB}x\left(\dot{u}_n^T+\dot{u}_n^\kappa\right)ds \tag{28}$$

Conversely, considering the grain portion O_eNP, one obtains accounting for Eq.(16),

$$\frac{\sqrt{3}}{2}B^2\Delta\dot{u}_{sl}+B\left(j_{2e}^{\kappa P}+j_{4e}^{\kappa N}\right)=\int_{GB}x\left(\dot{u}_n^T-\dot{u}_n^\kappa\right)ds \tag{29}$$

Being parallel, the pairs of GBs (f = 1 and 4) and (f = 2 and 5) have the same profile. In addition, due to the facts that $\kappa(s)$ is odd and $\kappa_e(s) = -\kappa(s)$, $j_{2e}^{\kappa P} = -j_5^{\kappa N}$ and $j_{4e}^{\kappa N} = -j_1^{\kappa P}$. Hence, summing Eqs (28) and (29) yields, via Eq (11)

$$\Delta\dot{u}_{sl} = -\frac{2}{\sqrt{3}B^2}\int_{GB} x\dot{u}_n^{\kappa} ds = -\frac{1}{2\sqrt{3}B^2}\mathcal{D}_b \int_{GB} x\nabla_s^2(\gamma\kappa) ds \tag{30}$$

i.e. also, via Eq. (23),

$$\Delta\dot{u}_{sl} = -\frac{2}{\sqrt{3}B^2}\mathcal{M}\gamma \int_{GB} x\kappa ds \tag{31}$$

Eq. (31) expresses the key feature that the amplitude of GB curvature is related to the amplitude of GB sliding. As suggested in Fig. 3, this relationship arises from the link between GB sliding and flux transfers across the GB. GB curvature is thus dynamically induced by strain rate. As $\dot{u}_{ne}^{\kappa} = -\dot{u}_n^{\kappa}$, there is no restriction on the form of the function $\dot{u}_n^{\kappa}(s)$ (in contrast to $\dot{u}_n^{T}(s)$ which, owing to grain rigidity, can only be the sum of a constant term and a term linear with x). There thus exists, for a given value of $\Delta\dot{u}_{sl}$, an infinity of functions $\kappa(s)$ that can comply with Eqs. (30) and (31). In particular, one of these functions may be such that $\kappa(s) = 0$ everywhere except inside the TJ cores where the applicability Eqs. (30) and (31) breaks down. In that case, the GB is flat in the part where curvature may be defined and the divergence of diffusion fluxes transiting from one grain to the other is non-null only inside TJ cores. The classical model assuming flat GBs is thus a particular case of a more general model accounting for GB curvature.

3.3. GB curvature, GB profile, and diffusion fluxes in conditions of Coble creep

Grain boundary profiles during straining can be calculated by solving Eq. (23), with Eq. (30) as boundary condition. We limit ourselves to small strain rate. In conditions of Coble creep, if GB curvature is small enough for allowing the approximation $ds \cong dx$, Eqs. (23) and (30) become

$$-\frac{1}{2}\gamma\mathcal{D}_b\frac{d^2\kappa}{dx^2}+\mathcal{M}\gamma\kappa=0 \tag{32}$$

$$\Delta\dot{u}_{sl}=-\frac{1}{\sqrt{3}}\frac{1}{B^2}\gamma\mathcal{D}_b\int_{-B}^{B}x\frac{d^2\kappa}{dx^2}dx\,, \tag{33}$$

The general solution of Eq. (32) complying with the condition that κ is odd may be expressed as

$$\kappa=\frac{1}{\sqrt{3}}am_b^2\sinh\left(\frac{1}{m_b}\frac{x}{B}\right)\frac{B^2\Delta\dot{u}_{sl}}{\gamma\mathcal{D}_b} \tag{34}$$

where $m_b=\sqrt{\frac{\mathcal{D}_b}{2\mathcal{M}B^2}}=1.29\frac{1}{R_G}\sqrt{\frac{\mathcal{D}_b}{\mathcal{M}}}$. (35)

Eq. (34) is written is such a way as to allow the use of the non-dimensional parameter m_b for analysing the influence of GB mobility in the deformation of a polycrystal with given grain size and given diffusivity, $\mathcal{D}_b$. The key-role played by parameter m_b will be highlighted in the following. Cahn and Taylor (Cahn and Taylor, 1994) also pointed out the role of the length scale $\sqrt{\frac{\mathcal{D}_b}{\mathcal{M}}}$ in their analysis of surface motion by coupling of surface diffusion and surface migration in a system in which the sole driving force is surface energy reduction. In Section 5.1, it will be shown that, according to experimental data for $\mathcal{D}_b$ and $\mathcal{M}$ in metals and ceramics that can be retrieved from the literature, $\sqrt{\frac{\mathcal{D}_b}{\mathcal{M}}}$ commonly amounts to a few nanometres, which means that $m_b \le 0.5$ even in the case of a nanocrystalline microstructure. We will thus analyse the role of m_b only in the range $0 \le m_b \le 0.5$.

Assuming that the integral in Eq. (34) may be carried out up to $x = \pm B$, i.e. also inside TJ cores, Eq. (34) yields, based on Eq. (33)

$$a = -\frac{3}{2}\frac{1}{m_b\left[\cosh\left(\frac{1}{m_b}\right) - m_b \sinh\left(\frac{1}{m_b}\right)\right]} \tag{36}$$

Unless $m_b = \infty$, $\cosh\left(\frac{1}{m_b}\right) - m_b \sinh\left(\frac{1}{m_b}\right) > 0$, hence $a < 0$. As $\sinh\left(\frac{1}{m_b}\right)$ tends to $\cosh\left(\frac{1}{m_b}\right)$ when m_b decreases, a tends to $-\frac{3}{2}\left(m_b \cosh\left(\frac{1}{m_b}\right)\right)^{-1}$ when $m_b \le 0.05$, which makes possible approximations that largely simplify the expressions of the equations ensuing from Eqs. (34) and (36). In the following, the full expressions will be given and the approximations valid for $m_b \le 0.05$ will be introduced only when useful.

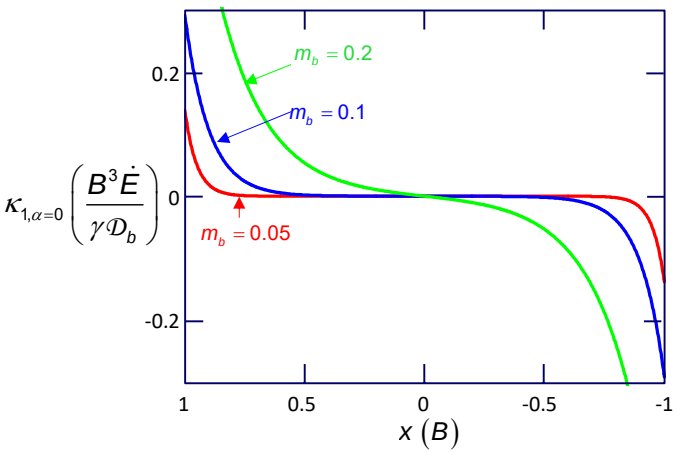

Figure 5: Curvature $\kappa_{1,\alpha=0}(x)$ calculated for m_b = 0.2, 0.1, and 0.05.

Figure 5 presents the curves for curvature $\kappa_{1,\alpha=0}(x)$ (i.e., in Fig. 2, for GB f = 1 when α = 0) calculated using m_b = 0.2, 0.1, and 0.05. Curvature tends to a maximum at TJs. Strictly speaking, the curves $\kappa_{1,\alpha=0}(x)$ have no meaning close to $x = \pm B$ because the concept of GB

curvature has no meaning inside the TJ core. Nevertheless, according to Eqs. (34) and (36), $\left(\kappa_{1\alpha=0}\right)_{x=\pm B}$ tends to $\pm\frac{3\sqrt{3}}{2}m_b\frac{B^3\dot{E}}{\gamma\mathcal{D}_b}$ when m_b decreases: the curvature at TJs thus tends to zero when $\mathcal{M}$ tends to ∞.

The slope of the profiles, denoted φ, can be derived from Eq. (34) as

$$\varphi_{f,\alpha}=\varphi_{f,\alpha}^0-\int_0^x\kappa_{f,\alpha}dx=\varphi_{f,\alpha}^0-\frac{1}{\sqrt{3}}am_b^3\cosh\left(\frac{x}{m_bB}\right)\frac{B^3\left(\Delta\dot{u}_{sl}\right)_{f,\alpha}}{\gamma\mathcal{D}_b} \tag{37}$$

where φ^0 is the slope at $x = 0$. The profile itself, $z(x)$, is obtained in turn as

$$z_{f,\alpha}=\int_0^x\varphi_{f,\alpha}dx=\varphi_{f,\alpha}^0x-\frac{1}{\sqrt{3}}am_b^4\sinh\left(\frac{x}{m_bB}\right)\frac{B^4\left(\Delta\dot{u}_{sl}\right)_{f,\alpha}}{\gamma\mathcal{D}_b}. \tag{38}$$

The three profiles, $z_{f,\alpha}\left(x\right)$, to be calculated thus differ by their slope at $x = 0$, $\varphi_{f\alpha}^0$. The latter three parameters can be identified based on three independent conditions:

- $\left(\varphi_{f\alpha}\right)_{x=B}=\left(\varphi_{(f+1)\alpha}\right)_{x=-B}$ for maintenance of the equilibrium dihedral angle at TJs (which brings two conditions)
- $\left(z_{f,\alpha}\right)_{x=B}-\left(z_{f+1,\alpha}\right)_{x=-B}+\left(z_{f+2,\alpha}\right)_{x=B}=0$ for consistency of the three departures from the initial, static TJ position.

For illustration, Figure 6a compares the profiles $z_{1,\alpha=0^\circ}\left(x\right)$ calculated for $m_b = 0.2$, 0.1, and 0.05 whereas Fig. 6b compares the curves $z_{1,\alpha=0^\circ}\left(x\right)$, $z_{6,\alpha=-45^\circ}\left(x\right)$, $z_{1,\alpha=-45^\circ}\left(x\right)$, and $z_{2,\alpha=-45^\circ}\left(x\right)$ calculated for $m_b = 0.1$. The profiles tend to be flat when $\mathcal{M}$ tends to infinity: in Fig. 6a, $\left(z_{1,\alpha=0^\circ}\right)_{x=\pm B}$ tends to $\frac{3\sqrt{3}}{2}m_b^2\frac{B^5\dot{E}}{\gamma\mathcal{D}_b}$ when m_b decreases whereas the slope at $x = 0$, $\left(\varphi_{1,\alpha=0^\circ}\right)_{x=0}$

, approximates as $\frac{3\sqrt{3}}{2} m_b^2 \frac{B^4 \dot{E}}{\gamma \mathcal{D}_b}$. The flat GB profiles considered classically thus correspond to the particular solution valid for the case $\mathcal{M} = \infty$.

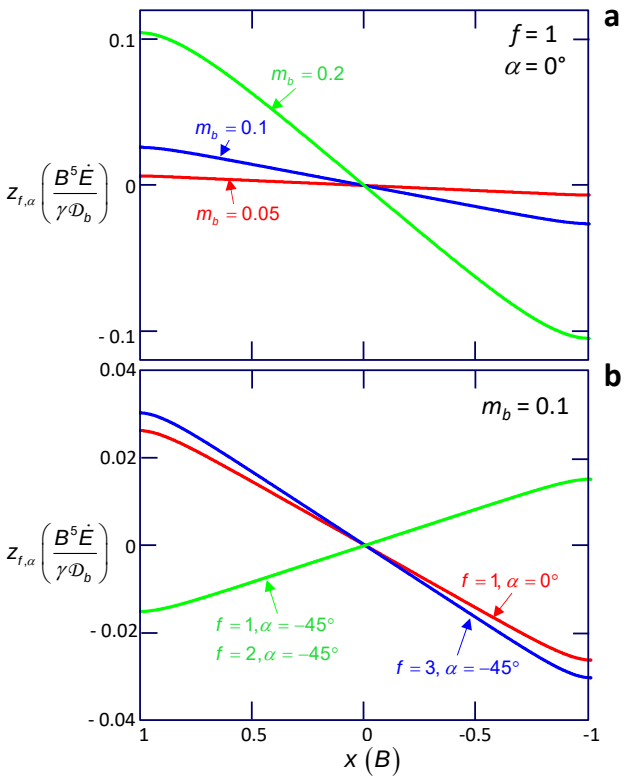

Figure 6: GB profiles $z_{1,\alpha}(x)$ calculated via Eqs. (37) and (38) (a) for m_b = 0.2, 0.1, and 0.05 with α = 0, and (b) for α = 0°, - 45°, and + 45° with m_b = 0.1.

The curves of Fig. 6b are used in Figure 7 for drawing the grain profiles (red curves) during deformation for the orientations α = 0°, α = -45° , and α = 90° with m_b = 0.1 (orientations α = 0°, α = -45° are the same as in Fig. 3). In the three cases, blue lines represent the GB position when equilibrium at rest has been recovered after unloading. GBs f = 3 and f = 6 remain flat when α = 0 (Fig. 7a) and α = 90° (Fig. 7c). The three cases are drawn in a somewhat different manner in order to illustrate the main features.

- In Fig. 7a, black lines represent the initial grains at equilibrium. Centroid O is considered static and four-pointed stars drawn in black and red localize the adjacent grain centroids (O and O_e) and the GB centroid (M) before and after deformation. Relative centroid velocities (sketched by red arrows) were calculated via Eq. (18) for an arbitrary finite strain rate. The GB sliding amplitude $\left(\Delta\dot{u}_{sl}\right)_{1,\alpha=0}$ is figured by a black arrow.
- In Fig. 7b, the GB slope at TJs during deformation is the same as at static equilibrium because $z_{1,\alpha=-45°} \equiv z_{2,\alpha=-45°}$ (Fig. 6b).
- In Fig. 7c, layers of thickness $2\dot{u}_n^T$ in grey shade represent mass addition along GBs $f = 1$ and $f = 2$, whereas dotted arrows sketch the directions of mass exchanges between GBs. As $\dot{u}_n^T$ is uniform along the GB, the frontiers of the shaded layers follow the same profile as the GB. When equilibrium at rest has been recovered after unloading, the profiles (blue lines) get an inclined orientation inside the layers of mass inflow. This feature will be discussed in Section 5.2.

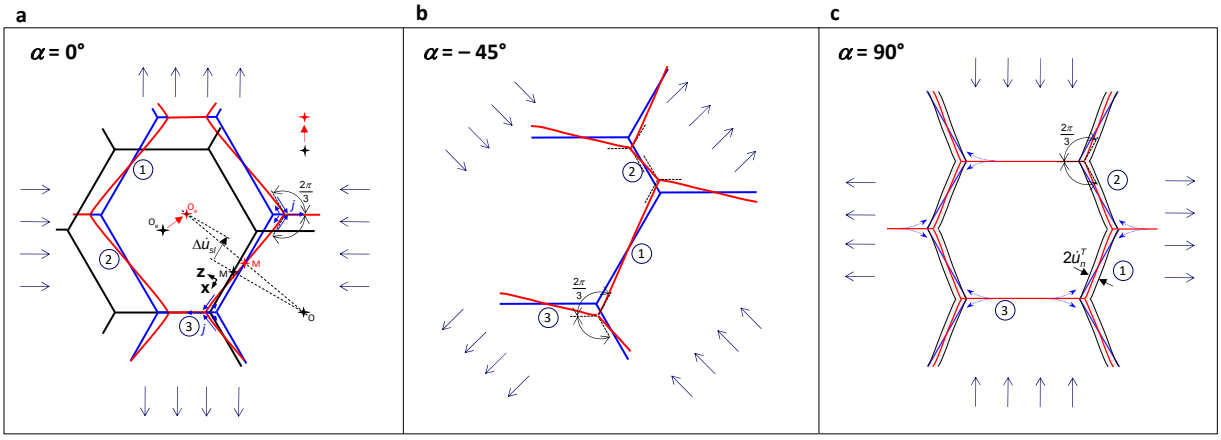

Figure 7: Grain shapes during deformation for $\alpha = 0°$, - 45°, and 90° (Fig. 2) with $m_b = 0.1$. The red curves are the GB profiles during straining whereas the blue lines are the GBs after relaxation to equilibrium at rest.

The diffusion fluxes in the reference grain driven by gradients of κ are, from Eq. (34),

$$j_{f,\alpha}^{\kappa} = -\frac{\mathcal{D}_b}{2}\frac{d(\gamma\kappa)}{dx} = -am_b \cosh\left(\frac{1}{m_b}\frac{x}{B}\right)B^2\dot{E}\sin\left(2\alpha - 2f\frac{\pi}{3}\right) \quad (39)$$

j^{κ} does not depend on γ. Conversely, the diffusion fluxes due to GB tractions are obtained via Eqs (20) as

$$j_{f,\alpha}^{T} = -\frac{1}{2}\int_0^x \Delta\dot{u}_z^O dx = -\sqrt{3}\cos\left(2\alpha - 2f\frac{\pi}{3}\right)\frac{x}{B}B^2\dot{E} \quad (40)$$

($j_f^T = 0$ at $x = 0$). $j_{f,\alpha}^T$ is thus linear with x. Figure 8a presents the curves for the total flux $\left(j^T(x) + j^{\kappa}(x)\right)_{f,\alpha=0}$ calculated using m_b = 0.2, 0.1, and 0.05. The shape of these curves is justified in Figure 8b by a sketch of the trajectories of the diffusion fluxes (the trajectories in Fig. 8b reproduce the trajectories drawn in Fig. 3a). Owing to the flux contributions due to the gradients of κ (Eq. (39)), the total flux presents sharp negative cusps at both TJs. As suggested in Fig. 8b, this results from the transfer of flux across the GB: flux transfer causes the total flux to be increased (i.e. to be more negative) close to TJ $x = -B$, and to be decreased (i.e. to be less positive, and even to become negative) close to TJ $x = B$. These phenomena concentrate in the part of the GB where curvature is the highest. In Fig. 7a, the orientation and magnitude of the main fluxes according to the curves of Fig. 8a are represented by blue arrows.

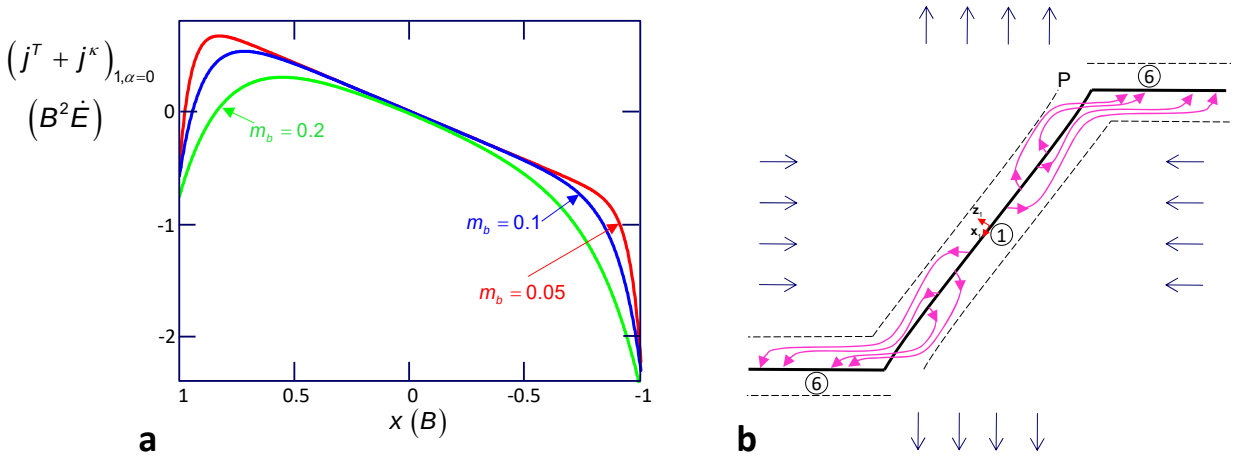

Figure 8: (a) total flux $\left(j^T + j^\kappa\right)_{1,\alpha=0}$ calculated for m = 0.2, 0.1, and 0.05. (b) sketch of the trajectories of the diffusion fluxes close to GB f = 1 with α = 0

3.4. Contributions to energy dissipation - apparent GB-viscosity

In the case of affine deformation under pure shear, the shear viscosity, G, is related to the dissipation rate per unit volume, $\dot{Q}$, via

$$G = \frac{\dot{Q}}{4\dot{E}^2} \tag{41}$$

$\dot{Q}$ is the sum of three contributions: $\dot{Q} = \dot{Q}^j + \dot{Q}^{mig} + \dot{Q}^{sl}$, where $\dot{Q}^j$ arises from diffusion fluxes, $\dot{Q}^{mig}$ arises from GB migration, and $\dot{Q}^{sl}$, arises from GB sliding.

- $\dot{Q}_b^j$ is calculated as

$$\begin{aligned}\dot{Q}_b^j &= \dot{Q}_b^T + \dot{Q}_b^\kappa = \frac{1}{V}\frac{2}{\mathcal{D}_b}\sum_{f=1}^{6}\int_{-B}^{B}\left(j_f^T + j_f^\kappa\right)^2 dx \\ &= \left\{\frac{2}{\sqrt{3}} + \frac{1}{\sqrt{3}}m_b^2 a^2\left[m_b \sinh\left(\frac{1}{m_b}\right)\cosh\left(\frac{1}{m_b}\right) + 1\right]\right\}\frac{B^3\dot{E}^2}{\mathcal{D}_b}.\end{aligned} \tag{42}$$

The two components of $\dot{Q}_b^j$ are thus uncoupled. The fact that $\dot{Q}_b^j$ does not depend on angle α follows from the relationships $\sum_{f=1}^{6}\cos^2\left(2\alpha - 2f\frac{\pi}{3}\right) = \sum_{f=1}^{6}\sin^2\left(2\alpha - 2f\frac{\pi}{3}\right) = 3$. The

first term in Eq. (42) is

$$\dot{Q}_b^T = \frac{2}{\sqrt{3}} \frac{B^3 \dot{E}^2}{\mathcal{D}_b}, \tag{43}$$

which, via Eq. (41), agrees with the shear viscosity calculated by Spingarn and Nix assuming flat GBs with free sliding (Kim et al., 2004; Spingarn and Nix, 1978).

- GB migration brings a dissipation power $\dot{u}_n^{mig} \frac{\Delta\mu}{\Omega} \equiv 2\dot{u}_n^{mig}\gamma\kappa$ on each unit area of the GB. This dissipation being equally shared between the two adjacent grains, $\dot{Q}_b^{mig}$ is obtained as

$$\begin{aligned} \dot{Q}_b^{mig} &= \frac{1}{V}\int_{GB} u_n^{mig}\gamma\kappa ds = \frac{1}{V}\mathcal{M}\gamma^2 \sum_{f=1}^{6}\int_{-B}^{B} \kappa_f^2 dx \\ &= \frac{1}{\sqrt{3}} m_b^2 a^2 \left[m_b \sinh\left(\frac{1}{m_b}\right)\cosh\left(\frac{1}{m_b}\right) - 1 \right] \frac{B^3\dot{E}^2}{\mathcal{D}_b} \end{aligned} \tag{44}$$

$\dot{Q}_b^{mig}$ thus differs only slightly from $\dot{Q}_b^{\kappa}$ (Eq. (42).

- Accounting for the intrinsic GB-viscosity associated to the nucleation and glide of disconnections, $\dot{Q}_{\text{intrinsic}}^{sl}$ is obtained as

$$\begin{aligned} \dot{Q}_{\text{intrinsic}}^{sl} &= \frac{1}{V}\frac{\eta^{\text{intrinsic}}}{2}\sum_{f=1}^{6}\int_{-B}^{B}\left(\Delta\dot{u}_{slf}\right)^2 dx \\ &= 2\sqrt{3}\eta^{\text{intrinsic}} B\dot{E}^2 = \frac{36}{\pi}\tilde{\eta}_b^{\text{intrinsic}} \frac{B^3\dot{E}^2}{\mathcal{D}_b} \end{aligned}. \tag{45}$$

($\tilde{\eta}_b^{\text{intrinsic}}$ is defined in Eq. (2)). Via Eq. (41), Eq. (45) reproduces the contribution to shear viscosity at zero strain ensuing from the equations developed by Kim et al (Kim et al., 2004).

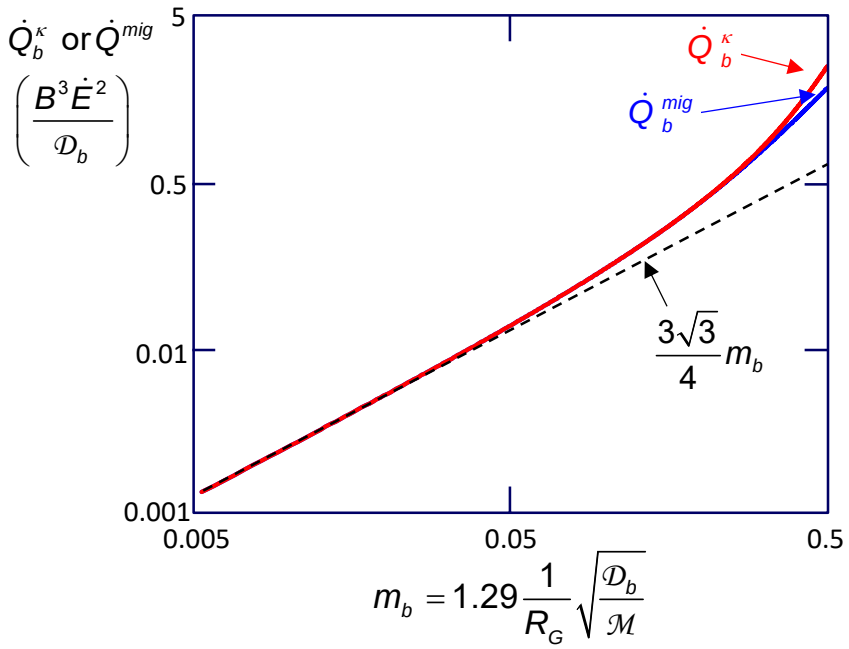

Figure 9: Variation of dissipation rates $\dot{Q}_b^{\kappa}$ and $\dot{Q}^{mig}$ as a function of m according to Eqs (42) and (44)

Figure 9 presents on a log-log scale the variation as a function of m_b of $\dot{Q}_b^{\kappa}$ (Eq. (42)) and $\dot{Q}_m^{mig}$ (Eq. (44)). $\dot{Q}_b^{\kappa}$ and $\dot{Q}_b^{mig}$ are very nearly identical as long as $m_b \le 0.05$. They tend to $\frac{3\sqrt{3}}{4} m_b \frac{B^3\dot{E}^2}{\mathcal{D}_b}$ when m_b decreases (dashed line). As m_b varies as B^{-1}, this means that $\dot{Q}_b^{\kappa}$ and $\dot{Q}_b^{mig}$ are closely proportional to R_G^2, in contrast to $\dot{Q}_b^{T}$ and $\dot{Q}^{sl}$ which vary as R_G^3 and R_G, respectively. The lower bound for the additional dissipation brought by strain-induced GB curvature is thus

$$\left(\dot{Q}_b^{\kappa} + \dot{Q}_b^{mig}\right)_{\text{lower bound}} = \frac{3\sqrt{3}}{2} m_b \frac{B^3\dot{E}^2}{\mathcal{D}_b} \tag{46}$$

Based on Eq. (45), Eq. (46) may be translated into a lower bound for a non-dimensional apparent GB-viscosity arising from the occurrence of GB curvature:

$$\left(\tilde{\eta}_b\right)_{lb} = \frac{\pi}{8\sqrt{3}} m_b = 0.23 m_b = 0.29 \frac{1}{R_G}\sqrt{\frac{\mathcal{D}_b}{\mathcal{M}}} \tag{47}$$

Eq. (47) highlights the key role played by GB mobility in diffusional deformation. It provides a precious clue on the value of apparent GB-viscosity η to be used in numerical simulation of diffusional deformation. This result will be further discussed in Section 5.1. As $\dot{Q}_b^{\kappa}$ and $\dot{Q}_b^{mig}$ vary as R_G^2 whereas $\dot{Q}_b^{T}$ vary R_G^3, it follows from Eqs. (43), (46), and (47) that, when GB-layer diffusion is dominant, the relative contribution to dissipation due to GB curvature decreases linearly with R_G. In contrast, the relative contribution due to GB curvature can be anticipated not to depend on R_G when bulk diffusion is dominant. This feature will be highlighted in Section 4.

4. Rotation of a grain embedded in a polycrystal

4.1. The classical model

Many authors have reported experimental evidence of the occurrence of random grain rotations during superplastic deformation of fine-grained polycrystals (Geckinli and Barrett, 1976; Harris et al., 1998; Hotz et al., 1975; Kashyap et al., 1985). Such grain rotations are intrinsic to the mechanism of diffusional deformation (Burton, 2002). Based on the latter mechanism, it has been predicted in the literature that, during deformation or during heat-treatment, a torque inducing the rotation of a grain can arise owing to an anisotropy of grain shape (Delannay and Brassart, 2020; Kim et al., 2009; Wheeler, 2010), to an anisotropy of GB tension, γ, (Harris et al., 1998; Kim et al., 2005; Moldovan et al., 2001), to an anisotropy of GB-viscosity, η, (Beere, 1978), or to the shear coupling effect (Cahn et al., 2006). In the present paper, the origin of the torque inducing grain rotation is left undetermined: the steady-state rotation of a grain with respect to its neighbours is viewed as “thought experiment” for the

assessment of the role of GB curvature and mobility in diffusional deformation. The rotation of a hexagonal grain embedded in a columnar polycrystal is a convenient case-study because, owing to the in-plane symmetry, rotation occurs without displacement of grain centroid. The grain rotation phenomenon was modelled by Harris et al (Harris et al., 1998) and Moldovan et al (Moldovan et al., 2001) assuming flat GBs with $\eta = 0$. The model was extended to the case $\eta \neq 0$ by Kim et al (Kim et al., 2005; Kim et al., 2009). Beeré (Beere, 1977), Kim et al (Kim et al., 2009) and Wheeler (Wheeler, 2010) also considered the simultaneous rotation of all grains in a lattice of columnar grains submitted to a uniform strain rate. Wheeler (Wheeler, 2010) demonstrated that such grain rotation brings no change of the shear viscosity unless grain shape is anisotropic and $\eta \neq 0$. The particular case of simultaneous rotation of the grains will be briefly treated in the Appendix.

Figure 10 outlines the grain rotation process in a columnar polycrystal with isometric grains. Capillary equilibrium implies (i) that GB shapes are such that the equilibrium dihedral angle $\psi = \frac{2\pi}{3}$ always maintains at TJs, and (ii) that GB curvature is null everywhere at rest: GB profiles at rest are figured by dotted straight lines. Notations *H*, *B*, O, M, P, N have the same meaning as in Section 3. Again, a Cartesian coordinate system with origin at M is defined by unit vectors **x** and **z**, with **z** oriented outward and **x** defined positive anticlockwise with respect to O. The angular velocity of the grain, $\dot{\theta}$, is also defined positive anticlockwise: $\dot{\theta}$ is thus positive in Fig. 10. The rotation of the grain with respect to its neighbours brings the existence of traction forces along its GBs. It follows from mechanical equilibrium that reaction forces act on the adjacent grains, which cause these grains to also rotate with respect to their neighbours, and so on for grains further away from the central grain. Hence, unless one considers that the

adjacent grains do not move because the diffusional deformation mechanism does not operate at their GBs, a model that considers a grain that rotates with respect to static neighbours does not yield to an exact solution complying with mechanical equilibrium. Nevertheless, according to variational principles, such a model constitutes an admissible kinematic approximation, which provides an upper bound for the dissipation power (Brassart and Delannay, 2019; Cocks, 1996; Delannay and Brassart, 2020). This upper bound approximation was implicit in previous work in literature: it is adopted in the following of this section.

If one assumes that adjacent grains do not rotate, the GB sliding velocity, i.e. the velocity jump between the two lattices at point M, is

$$\Delta \dot{u}_{sl} = \dot{u}_e^{lattice\,M} - \dot{u}^{lattice\,M} = -H\dot{\theta}\,. \tag{48}$$

Whatever the GB shape during grain rotation, $\Delta \dot{u}_{sl}$ is parallel to **x**, hence $T_{//} \equiv T_x$. If the torque bringing the rotation of the grain is constant, a stage will be reached during which GBs and TJs remain static while the grain is rotating. We define this stage as steady-state. The continuous black curves in Fig. 10 represent possible shapes for GB profiles at steady-state. These shapes will be justified in Fig. 14. It will be shown that it results from the assumption that adjacent grains are static

- that the position of TJs as well as the orientation of the tangents to the three GBs meeting at TJs are not affected by grain rotation,
- and that the “outgoing” GBs separating the six surrounding grains remain flat during the rotation of the central grain.

The GB profiles present central symmetry with respect to grain centroid and, as adjacent grains keep the same size, they present also central symmetry with respect to GB middle, M. $\kappa(x)$,

$\dot{u}_n^{\kappa}(x)$, and $\dot{u}_n^{mig}(x)$ are thus odd functions of *x*. In Fig. 10a, the continuous red lines aim at depicting the deformation incompatibilities arising from grain rotation: the rotation of the grain with respect to adjacent grains brings a normal velocity jump, $\Delta\dot{u}_n$, which, if GB curvature is not too large, may be approximated as linear with *x*:

$$\Delta\dot{u}_n = \dot{u}_n^T + \dot{u}_{ne}^T \cong x\dot{\theta}\,. \tag{49}$$

This velocity jump amounts to the insertion/withdrawal of wedges along the GB. The wedges are represented In Fig. 10b the by the gap between the dotted blue curve and the GB position during steady-state rotation (continuous black curve). As indicated by the blue arrows, accounting for the fact that $\dot{u}_n^T = \dot{u}_{ne}^T$ (Eq. (14)),

$$\dot{u}_n^T = \dot{u}_{ne}^T \cong x\frac{\dot{\theta}}{2} \tag{50}$$

If the effect of GB curvature is neglected, diffusion fluxes reduce to the contributions $\mathbf{J}^T$ and $\mathbf{J}_e^T$ in the case of Nabarro-Herring conditions, or j^T and j_e^T in the case of Coble conditions. $\mathbf{J}^T$ and $\mathbf{J}_e^T$ are sketched by red arrows in Fig. 10b. As emphasized in Section 4.3, these arrows do not represent the total fluxes $\mathbf{J}$ and $\mathbf{J}_e$ because the total fluxes involve also a contribution due to GB curvature.

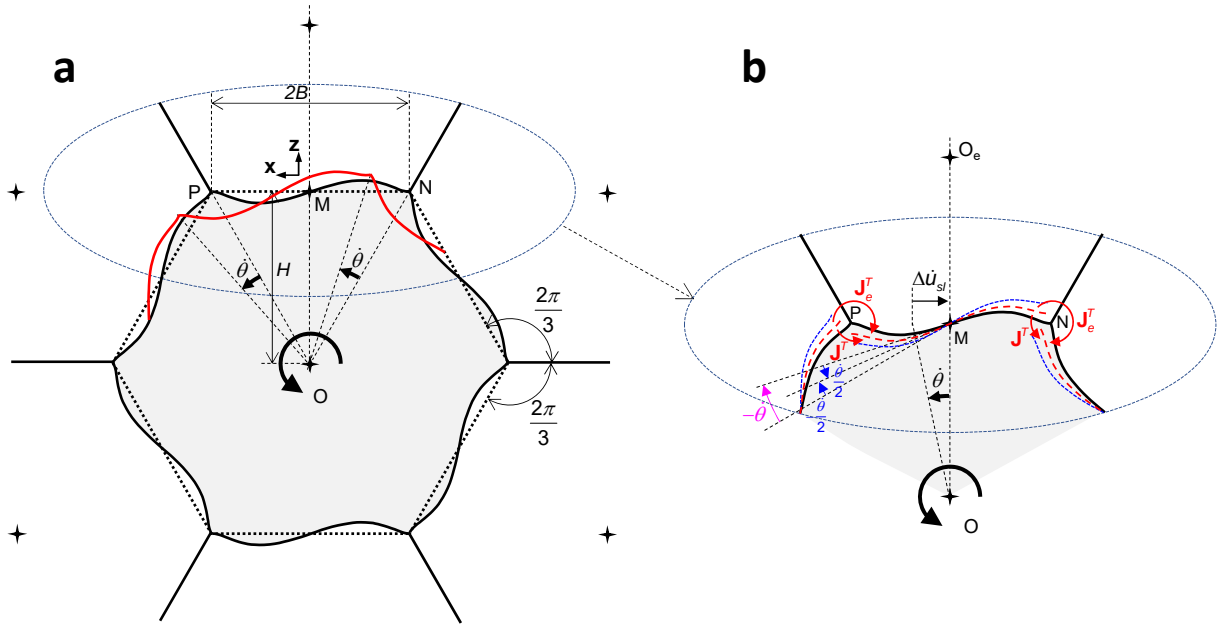

Figure 10: Rotation of a grain embedded in a columnar polycrystal.

Let us first consider the case of dominance of Coble conditions. The diffusion flux, $j^T(x)$, and the normal traction, $T_{bn}(x)$ (subscript b denotes Coble conditions), can be derived from Eq. (50) as

$$j^T = j_e^T = -\int \dot{u}_n^T dx = -\frac{1}{4}x^2\dot{\theta} + Cst_1 \tag{51}$$

and $$T_{bn} = \frac{2}{\mathcal{D}_b}\int j^T dx = \frac{2}{\mathcal{D}_b}\left(-\frac{1}{12}x^3\dot{\theta} + ax + Cst_2\right) \tag{52}$$

where Cst_1 and Cst_1 are integration constant. If adjacent grains are static, there is no velocity jump along the six outgoing GBs and normal tractions on these GBs are thus uniform. This implies that, if the activation barrier for the nucleation of disconnections at TJs is neglected, $T_{bn}(x = B) = T_{bn}(x = -B) = 0$. Hence,

$$T_{bn} = \frac{1}{6}\frac{1}{\mathcal{D}_b}\dot{\theta}\left(-x^3 + B^2 x\right) \tag{53}$$

and $$j^T = j_e^T = -\frac{1}{4}B^2\dot{\theta}\left(\frac{x^2}{B^2} - \frac{1}{3}\right) \quad (54)$$

Eq. (53) is identical to the equation derived by Kim et al (Kim et al., 2005). The contribution $\dot{Q}_b^T$ to the dissipation rate per unit volume that arises from the diffusive GB motions $\dot{u}_n^T$ and $\dot{u}_{ne}^T$ can then be calculated via two equivalent methods:

- either by equating $\dot{Q}_b^T$ to the work spent by the tractions on the GB: if $\eta_{\text{intrinsic}} = 0$, $T_{//} = 0$ and

$$\dot{Q}_b^T = \frac{1}{V}\left[\int_{GB} \dot{u}_n^T T_{bn} ds + \int_{GB} \dot{u}_{ne}^T T_{bn} ds\right] = \frac{2}{\sqrt{3}}\frac{1}{B^2}\int_{-B}^{B} \dot{u}_n^T T_{bn} dx \quad (55)$$

- or by equating $\dot{Q}^T$ to the dissipation associated to diffusion fluxes

$$\dot{Q}_b^T = \frac{1}{V}\frac{4}{\mathcal{D}_b}\int_{GB}\left[\left(j^T\right)^2 + \left(j_e^T\right)^2\right] ds = \frac{8}{\sqrt{3}}\frac{1}{B^2\mathcal{D}_b}\int_{-B}^{B} j^{T2} dx \quad (56)$$

Based on Eqs. (50), (53), and (54), both Eq. (55) and Eq. (56) yield

$$\dot{Q}_b^T = \frac{2}{45\sqrt{3}}\frac{B^3\dot{\theta}^2}{\mathcal{D}_b} \quad (57)$$

It can be verified that Eq. (57) agrees exactly with the value derived by Kim et al (Kim et al., 2005) for the dependence of $\dot{\theta}$ on the driving force for rotation when $\eta = 0$ (Eq. (23) in the reference). In their paper, Kim et al also discuss the (small) difference between their result and the results obtained via different approximations by Harris et al (Harris et al., 1998) and by Moldovan et al (Moldovan et al., 2001).

In the case of dominance of Nabarro-Herring conditions, the problem requires solving the Laplace equation, $\nabla^2\mu^T = 0$, inside the hexagonal grain and inside adjacent grains, subjected to Eqs. (9) and (50) as boundary conditions. Owing to the geometry of the problem,

accurate solutions for μ^T and for field of lattice flux $\mathbf{J}^T$ require resorting to a numerical method. By analogy with Eq. (57), $\dot{Q}_l^T$ (subscript l denotes Nabarro-Herring conditions) may be expressed as

$$\dot{Q}_l^T = q_l \frac{2}{45\sqrt{3}} \frac{B^2 \dot{\theta}^2}{\mathcal{D}_l} = q_l \frac{1}{B} \frac{\delta D_b}{D_l} \dot{Q}_b^T \tag{58}$$

where q_l is a non-dimensional factor. The principle of minimum dissipation implies that, according to Eq. (58), the transition between the two diffusion modes occurs when $B = q_l \frac{\delta D_b}{D_l}$. For the uniform deformation of a lattice of hexagonal grains, Raj and Ashby (Raj and Ashby, 1971) have calculated equivalent shear viscosities for the two modes of diffusion via an analytical method considering sliding along a corrugated GB. These shear viscosities, which they show to be consistent with previous work in the literature, translate into $q_l = 0.9$ in Eq. (58). This q_l value turns out to be fairly close to the value $q_l = 1.2$ that ensues from the full numerical calculations developed by Rudge (Rudge, 2018) for the shear viscosity of a regular lattice of hexagonal grains. No similar numerical solution of the Laplace equation has been proposed in the literature for the rotation of a grain with respect to its neighbours. For the latter case, we can only rely on the work of Moldovan et al (Moldovan et al., 2001) who applied the method of Raj and Ashby for analysing the phenomenon of grain rotation assuming either of the two modes of diffusion. The value derived by Moldovan et al for the critical grain size at the transition between the two diffusion modes translates into $q_l = 1.6$. In Section 4.4, this q_l value will be used as reference for comparison with the dissipation contributions arising from strain-rate-driven GB curvature.

4.2. GB curvature and transfer of diffusion fluxes across GBs during steady-state rotation

The definition of steady-state rotation implies a rotation centred in M of the GB with respect to the lattice of the rotating grain. The dashed red curve in Fig. 10b represents the GB position resulting only from the wedge insertion/withdrawal whereas the dotted blue curve shows where the GB would be positioned in the absence of GB rotation. In order to keep its steady-state position, the GB moves with respect to the lattice with a velocity $x\dot{\theta}$, i.e. with an angular velocity $-\dot{\theta}$ (magenta arrow). This GB velocity $x\dot{\theta}$ results from the sum of the three contributions:

$$\dot{u}_n^T + \dot{u}_n^\kappa + \dot{u}_n^{mig} = x\dot{\theta} \tag{59}$$

which, via Eq. (50), yields

$$\dot{u}_n^\kappa + \dot{u}_n^{mig} = x\frac{\dot{\theta}}{2} \tag{60}$$

Eq. (59) means that curvature governs simultaneously the rotation of the GB with respect to the lattice and the transfer across the GB of the matter, $\dot{u}_n^\kappa$, transported by diffusion driven by curvature. Via Eqs (11) and (17), Eq. (60) becomes

$$-\frac{\mathcal{D}_l}{\Omega}\left(\frac{\partial \mu^\kappa}{\partial \nu}\right)_{gb} + \frac{1}{2}\mathcal{D}_b\nabla_s^2\left(\gamma\kappa\right) - \mathcal{M}\gamma\kappa = x\frac{\dot{\theta}}{2}. \tag{61}$$

Previous authors who modelled the grain rotation process assumed $\Delta\dot{u}_n = 2\dot{u}_n^T = x\dot{\theta}$ and disregarded the GB migration bringing GB rotation (Harris et al., 1998; Kim et al., 2005; Moldovan et al., 2001).

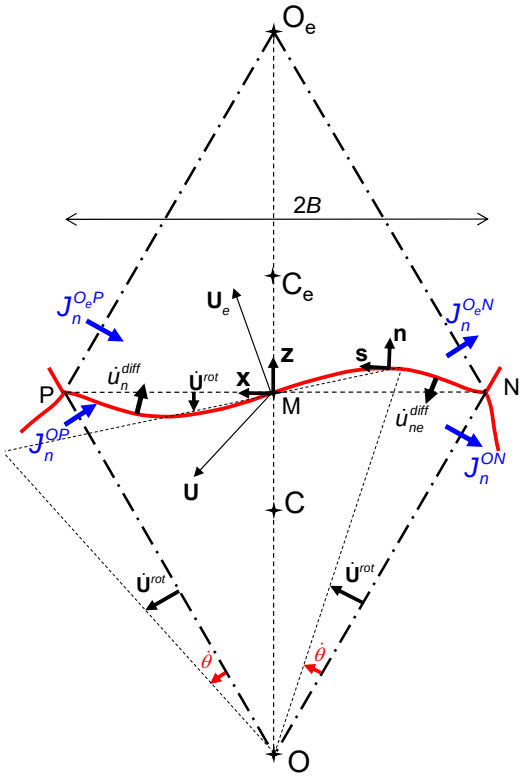

Figure 11. Parameters for calculating the displacement of sub-grain centroids.

Like in Section 3.2, based on Eq. (24), the relationship between the rotation velocity $\dot{\theta}$ and the distribution along the GB of the diffusional GB velocities $\dot{u}_n^{\kappa}(x) = -\dot{u}_{ne}^{\kappa}(x)$ can, be established by calculating the displacement of the centroids, C and C_e, of the two adjacent sub-grains OPN and O_eNP represented in Fig. 11 (in contrast to Fig. 4, Fig. 11 depicts bulk fluxes **J**, i.e. Nabarro-Herring conditions). Let us first apply Eq. (24) on sub-grain OPN. In Fig. 11, the arrows labelled $\dot{\mathbf{U}}^{rot}$ represent the velocity of the external surface of sub-grain OPN, and the dashed triangle represents the displacement brought by the rotation of the grain. It can be verified that, in direction *x*,

$$\frac{1}{V}\left(\int_{OP} U_x\left(\dot{\mathbf{U}}^{rot}\cdot\mathbf{n}\right)dS + \int_{PN} U_x\left(\dot{\mathbf{U}}^{rot}\cdot\mathbf{n}\right)dS + \int_{NO} U_x\left(\dot{\mathbf{U}}^{rot}\cdot\mathbf{n}\right)dS\right) = \frac{2}{3}H\dot{\theta}\,. \tag{62}$$

As $\frac{2}{3}H\dot{\theta}$ is the velocity of centroid C, the balance of the other contributions to the integral on

the righthand side of Eq. (24) is null:

$$\int_{OP} x\left(\mathbf{J}\cdot\mathbf{n}\right)dS + \int_{GB} x\dot{u}_n^{diff}\,dS + \int_{NO} x\left(\mathbf{J}\cdot\mathbf{n}\right)dS = 0 \tag{63}$$

The normal component of the diffusion flux across faces OP and ON, $J_n = J_n^T + J_n^\kappa$, is sketched by blue arrows in Fig. 11. In the case of dominance of Coble conditions, $\frac{\delta J_n^T}{2} \equiv j_n^T$ and we may write, accounting for Eq. (54),

$$\int_{OP} x\left(\mathbf{J}\cdot\mathbf{n}\right)ds + \int_{NO} x\left(\mathbf{J}\cdot\mathbf{n}\right)ds \cong 2B\left[\left(j^T\right)_{x=B} + \frac{\delta J_n^\kappa}{2}\right] = 2B\left(-\frac{1}{6}B^2\dot{\theta} + \frac{\delta J_n^\kappa}{2}\right) \tag{64}$$

In the case of Nabarro-Herring conditions, $2B\left(-\frac{1}{6}B^2\dot{\theta} + \frac{\delta J_n^\kappa}{2}\right)$ may be considered as a valid approximation because $\mathbf{J}$ is then expected to be significant only in the vicinity of TJs. Hence, whatever the dominant diffusion mode, Eq. (63) yields

$$-2B\left(\frac{1}{6}B^2\dot{\theta} - \frac{\delta J_n^\kappa}{2}\right) + \int_{GB} x\left(\dot{u}_n^T + \dot{u}_n^\kappa\right)ds = 0 \tag{65}$$

Similarly, the application of Eq. (24) on sub-grain O_ePN yields

$$2B\left(\frac{1}{6}B^2\dot{\theta} - \frac{\delta J_{ne}^\kappa}{2}\right) + \int_{GB} x\left(\dot{u}_n^T - \dot{u}_n^\kappa\right)ds = 0 \tag{66}$$

As $J_n^\kappa = -J_{ne}^\kappa$, it follows from Eqs. (11), (65), and (66)

$$\dot{\theta} = \frac{3}{B^3}\int_{GB} x\dot{u}_n^\kappa ds = \frac{3}{B^3}\int_{GB} x\left(-\frac{\mathcal{D}_l}{\Omega}\left(\frac{\partial\mu^\kappa}{\partial\nu}\right)_{gb} + \frac{1}{2}\mathcal{D}_b\nabla_s^2\left(\gamma\kappa\right)\right)ds \tag{67}$$

Eq. (67) is the collateral of Eq. (30). Again, the classical model assuming flat GBs with diffusion fluxes transiting only across TJ cores corresponds to a particular function $\dot{u}_n^\kappa\left(s\right)$ complying with Eq. (67).

4.3. GB curvature and GB profiles

In this Section, solutions based on Eqs (61) and (67) are developed while considering either the dominance of GB-layer diffusion or the dominance of bulk diffusion. Subscripts b and l are used for distinguishing the two cases. The absence of subscript means that the expression is valid for both cases. For the case of bulk diffusion, a method is proposed that brings an approximate expression for κ presenting a similar analytical form as for the case of GB-layer diffusion. This similarity will make possible a comprehensive view of the rotation process across the full range of diffusion conditions.

In conditions of dominance of GB-layer diffusion, Eqs (61) and (67) reduce to

$$\frac{1}{2}\gamma\mathcal{D}_b\frac{d^2\kappa_b}{dx^2} - \mathcal{M}\gamma\kappa_b = x\frac{\dot{\theta}}{2} \tag{68}$$

and

$$\int_{-B}^{B} x\frac{d^2\kappa_b}{dx^2}dx = \frac{2}{3}\frac{B^3}{\gamma\mathcal{D}_b}\dot{\theta}\,, \tag{69}$$

The general solution of Eq. (68) complying with the condition that κ is odd can be written

$$\kappa_b = \left[a_b \sinh\left(\frac{1}{m_b}\frac{x}{B}\right) - \frac{1}{2}\frac{x}{B}\right]\frac{B\dot{\theta}}{\gamma\mathcal{M}} \tag{70}$$

with, like Eq. (35),

$$m_b = \frac{1}{\sqrt{2}}\frac{1}{B}\sqrt{\frac{\mathcal{D}_b}{\mathcal{M}}}\,. \tag{71}.$$

Eqs. (69) to (71) yield

$$a_b = \frac{1}{6}\frac{1}{m_b\left[\cosh\left(\frac{1}{m_b}\right) - m_b\sinh\left(\frac{1}{m_b}\right)\right]} \tag{72}$$

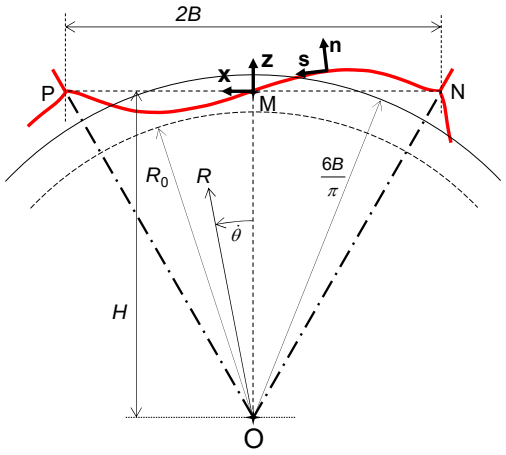

Figure 12. Parameters for the solution of the Laplace equation in polar coordinates

In conditions of dominance of bulk diffusion, the problem requires solving the Laplace equation $\nabla^2 \mu^\kappa = 0$ inside a regular hexagon, subjected to Eqs. (61) and (67) as boundary conditions. A precise solution can be obtained only via a numerical method. In the present paper, we proceed via an analytical approximation based on polar coordinates (R, θ) centred at O (Fig. 12). The approximation consists in applying conditions Eqs. (61) and (67) along the arc of circle of length 2B defined as $\left(R = \frac{6B}{\pi},\ -\frac{\pi}{6} \le \theta \le \frac{\pi}{6} \right)$: we thus approximate $x \cong s = \frac{6}{\pi} B\theta$ and $\left(\frac{\partial \mu^\kappa}{\partial \nu} \right)_{gb} \cong \left(\frac{\partial \mu^\kappa}{\partial R} \right)_{R=\frac{6B}{\pi}}$. Eqs. (61) and (67) then translate into

$$\frac{\mathcal{D}_l}{\mathcal{M}} \left(\frac{\partial \mu^\kappa}{\partial R} \right)_{R=\frac{6B}{\pi}} + \mu^\kappa_{R=\frac{6B}{\pi}} = -\frac{1}{2} \frac{6}{\pi} \theta \frac{\Omega B \dot{\theta}}{\mathcal{M}} \tag{73}$$

and

$$\int_{-\frac{\pi}{6}}^{\frac{\pi}{6}} \theta \left(\frac{\partial \mu^\kappa}{\partial R} \right)_{R=\frac{6B}{\pi}} d\theta = -\frac{1}{3} \left(\frac{\pi}{6} \right)^2 \frac{\Omega B \dot{\theta}}{\mathcal{D}_l} \tag{74}$$

As the gradients of diffusion potential due to GB curvature vanish beyond a certain distance from the GB, we denote R_0 a critical radius from centroid O below which bulk diffusion fluxes

due to GB curvature are null: $J_R^\kappa = -\frac{\mathcal{D}_l}{\Omega}\frac{\partial \mu^\kappa}{\partial R} = 0$ when $R \le R_0$ (Fig. 12). A general solution of the Laplace equation complying the latter condition as well as with Eq. (73) may be written

$$\mu^\kappa = 0 \text{ for } R \le R_0 \tag{75}$$

and $$\mu^\kappa = \left[\sqrt{2}a_l \cos\left(\frac{1}{m_l}\ln\frac{R}{R_0}\right)\sinh(\frac{1}{m_l}\frac{6\theta}{\pi}) - \frac{1}{2}\frac{6\theta}{\pi}\right]\frac{B\Omega\dot{\theta}}{\mathcal{M}} \text{ for } R > R_0 \tag{76}$$

with $$R_0 = \frac{6}{\pi}B\exp\left(-m_l\frac{\pi}{4}\right), \text{ i.e. } \cos\left[\frac{1}{m_l}\ln\left(\frac{6}{\pi}\frac{B}{R_0}\right)\right] = \frac{1}{\sqrt{2}} \tag{77}$$

and $$m_l = \frac{\pi}{6}\frac{1}{B}\frac{\mathcal{D}_l}{\mathcal{M}} = \frac{\pi\sqrt{2}}{6}\frac{\mathcal{D}_l}{\mathcal{D}_b}\sqrt{\frac{\mathcal{D}_b}{\mathcal{M}}}m_b \tag{78}$$

The crudeness of the approximations underlying Eqs. (75) and (76) is reflected by the discontinuities of μ^κ at $R = R_0$ and at $\theta = \pm\frac{B}{R} = \pm\frac{\pi}{6}$ when $R > R_0$. Eqs. (74) and (76) yield

$$a_l = \frac{1}{6}\frac{1}{m_l\left[\cosh\left(\frac{1}{m_l}\right) - m_b\sinh\left(\frac{1}{m_l}\right)\right]} \tag{79}$$

Based on Eq. (76), GB curvature then expresses

$$\kappa_l = \frac{\mu_{gb}^\kappa}{\Omega\gamma} = \left[a_l\sinh\left(\frac{1}{m_l}\frac{x}{B}\right) - \frac{1}{2}\frac{x}{B}\right]\frac{B\dot{\theta}}{\gamma\mathcal{M}} \tag{80}$$

Eqs. (70) and (80) show that κ tends to zero when $\mathcal{M}$ tends to ∞: the assumption that GBs remain flat during grain rotation is thus a particular case of the more general model accounting for GB curvature. This indicates that previous models based on the classical hypothesis of flat GBs (Harris et al., 1998; Kim et al., 2005; Moldovan et al., 2001) involved also the implicit assumption that GB mobility is infinite. Eqs. (70) and (76) yield, via Eq. (11), the same expression for the diffusive GB velocities driven by curvature gradients:

$$\dot{u}_n^{\kappa} = -\dot{u}_{en}^{\kappa} = a\sinh\left(\frac{1}{m}\frac{x}{B}\right)B\dot{\theta} \tag{81}$$

Although more approximate than Eq. (70), Eq. (80) will be considered as correct enough for the purpose of apprehending the essential of the rotation phenomenon across the full range of diffusion conditions. The only difference between Eqs. (70) and (80) is the different definition of parameters m_b and m_l (Eqs. (71) and (78)). As $\frac{\mathcal{D}_b}{\mathcal{D}_l} \approx 1\mu\text{m}$ whereas $\sqrt{\frac{\mathcal{D}_b}{\mathcal{M}}} \approx 1\text{nm}$ (confer Section 5.1), it follows from Eq. (78) that $m_l << m_b$. m_b and m_l both vary as R_G^{-1} whereas dominance of bulk diffusion is favoured when R_G increases at a given temperature. In the following, the outcomes of Eqs. (70) and (80) are analysed over the range $0 \le m \le 0.5$. The lowest part of this range is thus representative for the case of dominance of bulk diffusion and the highest part for the case of the dominance of GB-layer diffusion.

Figure 13 presents the curves $\kappa(x)$ in units of $\frac{B\dot{\theta}}{\gamma\mathcal{M}}$ for m (i.e. m_b or m_l) = 0.2, 0.1, and 0.05. According to Eq. (17), Fig. 13 also represents the variation of the migration velocity $\dot{u}_n^{mig}$ along the GB. The linear variation of κ in the central part of the GB is brought by the rotation of the GB around M. When m decreases (e.g. because grain size increases), the departure from this linear variation localises closer to TJs. When $m \le 0.05$, κ tends to $\pm\frac{1}{6m}\frac{B\dot{\theta}}{\gamma\mathcal{M}}$ when x tends to $\pm B$ (again, strictly speaking, κ has no meaning at $x = \pm B$).

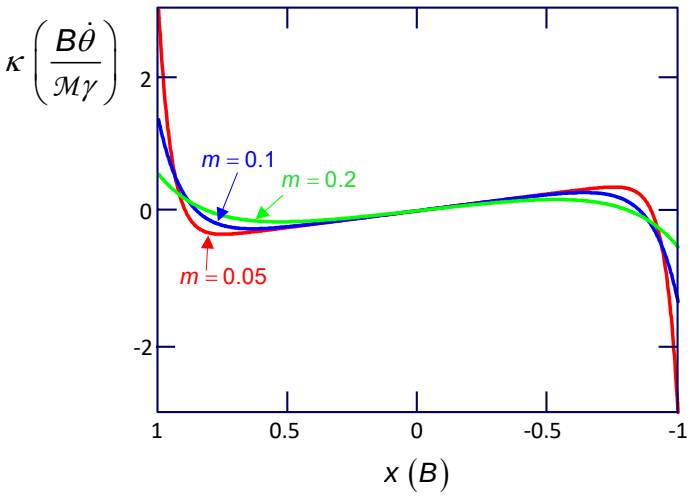

Figure 13. Curvature $\kappa(x)$ according to Eqs. (34) and (80) for m = 0.2, 0.1, and 0.05.

Based on Eqs. (70) and (80), the slope of the profile expresses

$$\varphi = \varphi^0 - \int_0^x \kappa dx = \varphi^0 - \left[am\cosh\left(\frac{1}{m}\frac{x}{B}\right) - \frac{1}{4}\left(\frac{x}{B}\right)^2 \right]\frac{B^2\dot{\theta}}{\gamma\mathcal{M}} \tag{82}$$

where φ° is the slope at GB centroid M. The profile itself is obtained as

$$z = \int_0^x \varphi dx = \varphi^0 x - \left[am^2 \sinh\left(\frac{x}{m\,B}\right) - \frac{1}{12}\left(\frac{x}{B}\right)^3 \right]\frac{B^3\dot{\theta}}{\gamma\mathcal{M}}. \tag{83}$$

By symmetry, GB profiles must comply with the boundary condition $z(x) = 0$ at $x = \pm B$. It thus follows from Eq. (83) that the slope of the profile at $x = 0$ is

$$\varphi^0 = \left[am^2 \sinh\left(\frac{1}{m}\right) - \frac{1}{12} \right]\frac{B^2\dot{\theta}}{\gamma\mathcal{M}}. \tag{84}$$

and the equation for the profile becomes

$$z = \left\{ am^2 \left[\sinh\left(\frac{1}{m}\right)\frac{x}{B} - \sinh\left(\frac{x}{mB}\right) \right] - \frac{1}{12}\left[\frac{x}{B} - \left(\frac{x}{B}\right)^3 \right] \right\}\frac{B^3\dot{\theta}}{\gamma\mathcal{M}}. \tag{85}$$

Figure 14 presents the curves for $z(x)$ in units of $\frac{B^3\dot{\theta}}{\gamma\mathcal{M}}$ for m = 0.2, 0.1, and 0.05. Strikingly, the

slope at TJs, i.e. the angle of rotation of TJs at steady state, is null: $(\varphi)_{x=\pm B} = 0$. The absence of rotation of TJs indicates that outgoing GBs remain flat, which is consistent with the absence of rotation the adjacent grains (this point is further highlighted in Section 4.4). The GB profiles presented in Figs 10, 11, and 12 have been drawn based on the curve for m = 0.1 in Fig. 14. As shown in the Appendix, the profiles $z(x)$ would be completely different if all grains rotate simultaneously with the same angular velocity.

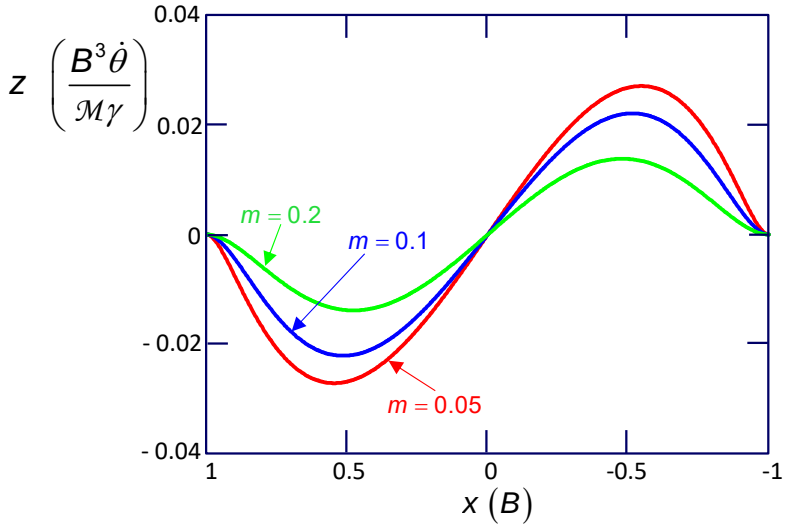

Figure 14. GB profile $z(x)$ according to Eq. (85) for m = 0.2, 0.1, and 0.05.

4.4. Diffusion fluxes

In the case of GB-layer diffusion, the flux components driven by curvature gradients are obtained via Eqs. (70) as

$$j^{\kappa} = -j_e^{\kappa} = -\frac{\mathcal{D}_b}{2}\frac{d(\gamma\kappa)}{dx} = -m_b^2\left[a_b\frac{1}{m_b}\cosh\left(\frac{1}{m_b}\frac{x}{B}\right) - \frac{1}{2}\right]B^2\dot{\theta} \qquad (86)$$

Figure 15a presents the curves $j^{\kappa}(x)$ in units of $B^2\dot{\theta}$ for m_b = 0.2, 0.1, and 0.05. j^{κ} is slightly positive in the middle of the GB and presents sharp negative cusps at both TJs. When m_b

decreases, $\left(j^{\kappa}\right)_{x=0}$ tends to $\frac{1}{2}m_b^2B^2\dot{\theta}$, whereas $\left(j^{\kappa}\right)_{x=\pm B}$ tends to $-\frac{1}{6}B^2\dot{\theta}$. Reference to Eq. (54) shows that this means $\left(j^{\kappa}\right)_{x=\pm B} \cong \left(j^{T}\right)_{x=\pm B}$. Figure 15b presents the curves for j^T according to Eq. (54), together with the curves for the total diffusion fluxes, $j^T + j^{\kappa}$ and $j_e^T + j_e^{\kappa}$, calculated using m_b = 0.1. GB curvature brings the total diffusion flux to be larger on the internal side of the rotating grain than on the external side. In particular, $\left(j_e^T + j_e^{\kappa}\right)_{x=\pm B} \cong 0$. The GB curvature close to TJs thus brings the total diffusion flux on the external side to cross the GB close to the TJ in such a way as to circumvent the TJ on the internal side. This is consistent with the fact that outgoing GBs are flat and can thus not be crossed by diffusion fluxes.

In the case of bulk diffusion, the expression of μ^{κ} by Eq. (76) is too approximate to allow accurate mapping of the $\mathbf{J}^{\kappa}$ field inside the grain. Nevertheless, the curves for j and j_e presented in Fig 15 suggest the outlines of a map for lattice fluxes **J** and $\mathbf{J}_e$. Fig. 16 presents such a map drawn qualitatively in accordance with Figs. 10, 14, and 15. Like j and j_e in Fig. 15, **J** and $\mathbf{J}_e$ are taken to change direction at $X \simeq \pm 0.6B$: this point corresponds to either a saddle or a minimum in the μ field. **J** and $\mathbf{J}_e$ cross the GBs close to TJs in such a way as to flow only on the internal side of the TJ core. Notice that the mapping of **J** and $\mathbf{J}_e$ in Fig. 15 does not invalidate the red arrows drawn in Fig. 10b for sketching the lattice flux components $\mathbf{J}^T$ and $\mathbf{J}_e^T$.

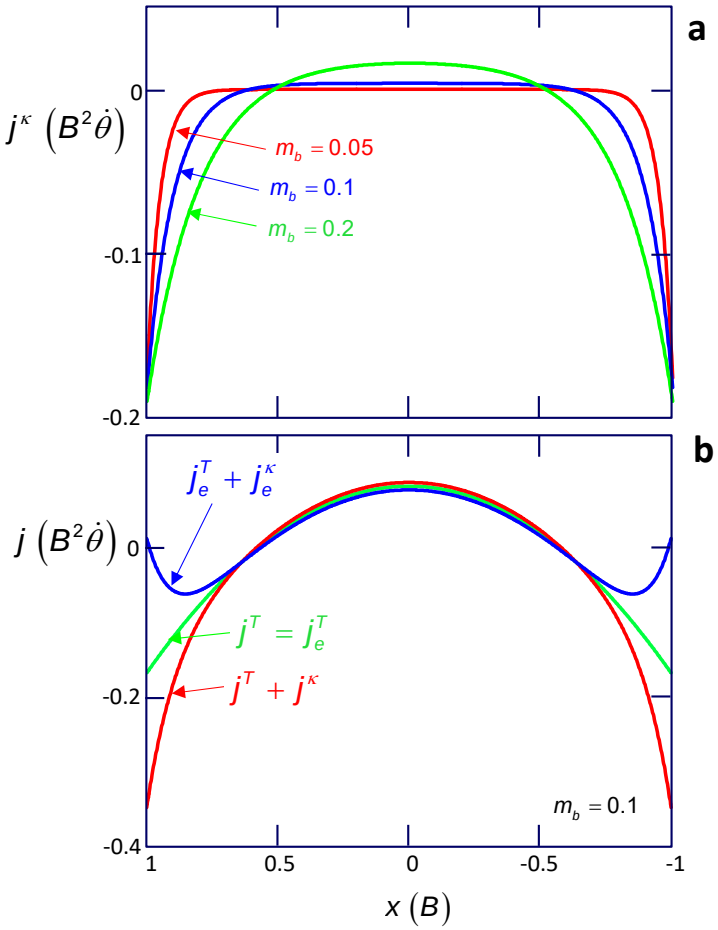

Figure 15: (a) Diffusion flux $j^{\kappa}(x)$ for m_b = 0.2, 0.1, and 0.05 ; (b) total diffusion fluxes, $j^T + j^{\kappa}$ and $j_e^T + j_e^{\kappa}$, calculated using m_b = 0.1.

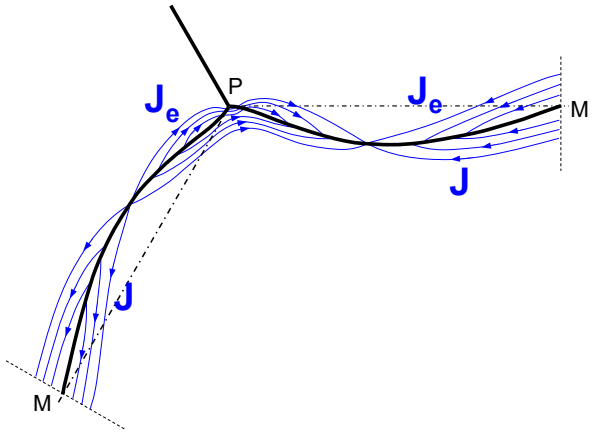

Figure 16: Outlines of a map of bulk diffusion fluxes **J** and $\mathbf{J}_e$

4.5. Contributions to energy dissipation

It must be remembered that the assumption that adjacent grains do not rotate constitute a kinematical approximation which can yield only an upper bound for the dissipation power. Like in Section 3.4, we may distinguish four contributions to the dissipation power per unit volume: $\dot{Q} = \dot{Q}^T + \dot{Q}^\kappa + \dot{Q}^{mig} + \dot{Q}^{sl}_{\text{intrinsic}}$.

- $\dot{Q}^T_b$ and $\dot{Q}^T_l$ have already been expressed in Eqs. (57) and (58).
- Like $\dot{Q}^T_b$, $\dot{Q}^\kappa$ can be obtained either by calculating the work spent by the tractions on the GB (Eq. (55)), or by calculating the dissipation brought by diffusion fluxes (Eq. (56)). The first method writes

$$\begin{aligned}\dot{Q}^T + \dot{Q}^\kappa &= \frac{1}{V}\left[\int_{GB} \dot{u}_n^{diff}\left(T_n + \gamma\kappa\right)ds + \int_{GB} \dot{u}_{ne}^{diff}\left(T_n - \gamma\kappa\right)ds\right] \\ &= \dot{Q}^T + \frac{2}{\sqrt{3}}\frac{1}{B^2}\int_{-B}^{B} \dot{u}_n^\kappa \gamma\kappa dx\end{aligned} \tag{87}$$

Using Eq. (81) for $\dot{u}_n^\kappa$ and Eqs. (70) or (80) for κ, one obtains whatever the diffusion mode,

$$\dot{Q}^\kappa = \frac{2}{\sqrt{3}}\left\{a^2\left[m\sinh\left(\frac{1}{m}\right)\cosh\left(\frac{1}{m}\right) - 1\right] - \frac{1}{6}\right\}\frac{B\dot{\theta}^2}{\mathcal{M}} \tag{88}$$

For $\dot{Q}^\kappa_l$, the second method cannot be used owing to the lack of a precise expression for the fields $\mathbf{J}^\kappa$ and $\mathbf{J}^\kappa_e$. For $\dot{Q}^\kappa_b$, the method writes

$$\begin{aligned}\dot{Q}^T_b + \dot{Q}^\kappa_b &= \frac{1}{V}\frac{2}{\mathcal{D}_b}\int_{GB}\left[\left(j^T + j^\kappa\right)^2 + \left(j^T_e + j^\kappa_e\right)^2\right]ds \\ &= \dot{Q}^T_b + \frac{8}{\sqrt{3}}\frac{1}{B^2\mathcal{D}_b}\int_{-B}^{B} j^{\kappa 2} dx\end{aligned} \tag{89}$$

Coupling with Eq.(86), Eq. (89) yields

$$\dot{Q}^\kappa_b = \frac{2}{\sqrt{3}}\left\{a_b^2\left[1 + m_b\cosh\left(\frac{1}{m_b}\right)\sinh\left(\frac{1}{m_b}\right)\right] - 2a_b m_b^2\sinh\left(\frac{1}{m_b}\right) + \frac{1}{2}m_b^2\right\}\frac{B\dot{\theta}^2}{\mathcal{M}} \tag{90}$$

Eq. (90) differs from Eq. (88). The difference is however small as long as $m_b < 0.1$ (see Fig.

17 below). We believe that it may be ascribed to the inaccuracies in the integrals and derivatives due to the approximation $s \cong x$.

- Whatever the diffusion mode, $\dot{Q}^{mig}$, can be obtained via Eq. (17) coupled to either Eq. (70) or Eq. (80):

$$\begin{aligned}\dot{Q}^{mig} &= -\frac{2}{V}\int_{GB} u_n^{mig}\gamma\kappa ds = \frac{2}{V}\mathcal{M}\gamma^2\int_{GB}\kappa^2 ds \\ &= \frac{2}{\sqrt{3}}\left\{a^2 B\left[m\sinh\left(\frac{1}{m}\right)\cosh\left(\frac{1}{m}\right)-1\right]-\frac{1}{6}\right\}\frac{B\dot{\theta}^2}{\mathcal{M}}\end{aligned} \tag{91}$$

According to Eq. (88), $\dot{Q}^{mig}$ is equal to $\dot{Q}_b^{\kappa}$, but according to Eq. (90) $\dot{Q}^{mig}$ differs somewhat from $\dot{Q}_b^{\kappa}$.

- $\dot{Q}^{sl}_{\text{intrinsic}}$ is obtained via Eqs (1) and (48),

$$\dot{Q}^{sl}_{\text{intrinsic}} = \frac{1}{V}\int_{GB} T_{//}\Delta\dot{u}^{sl} ds = \frac{2}{\sqrt{3}B}\eta_{\text{intrinsic}}\left(\Delta\dot{u}^{sl}\right)^2 = 2\sqrt{3}\,\eta_{\text{intrinsic}} B\dot{\theta}^2 \tag{92}$$

It follows from Eqs. (88), (90) and (91) that, when *m* decreases,

$$\dot{Q}^{\kappa} \cong \dot{Q}^{mig} \to \frac{1}{18\sqrt{3}}\frac{1}{m}\frac{B\dot{\theta}^2}{\mathcal{M}} \tag{93}$$

As $m \propto B^{-1}$, this means that $\dot{Q}_l^{\kappa}$, $\dot{Q}_b^{\kappa}$, $\dot{Q}_l^{mig}$, and $\dot{Q}_b^{mig}$ all vary nearly as B^2, like $\dot{Q}_l^{T}$ (Eq. (58)).

Given an average grain size, if $\dot{Q}^{sl}_{\text{intrinsic}}$ is neglected, the temperature dependence of the dissipation rate, $\dot{Q} = \dot{Q}^{T} + \dot{Q}^{\kappa} + \dot{Q}^{mig}$, is determined by the dependence on temperature of the characteristic lengths $\frac{\delta D_b}{D_l}$ and $\sqrt{\frac{\mathcal{D}_b}{\mathcal{M}}}$ (which combine into the characteristic length $\frac{\mathcal{D}_l}{\mathcal{M}}$). In principle, this dependence can be derived from the exponential pre-factor and the activation energy in the Arrhenius law for δD_b, D_l, and $\mathcal{M}$. Reliable data for this set of parameters in

metals and ceramics in the temperature range at which diffusional deformation is expected to prevail are however scarce in the literature. For $\frac{\delta D_b}{D_l}$, it is commonly admitted in the literature devoted to creep and sintering that the transition between dominance of bulk diffusion and dominance GB-layer diffusion occurs at a grain size $R_G \simeq \frac{\delta D_b}{D_l}$ of the order of one μm. The activation energy being lower for δD_b than for D_l, the transition occurs at a critical grain size that decreases when temperature increases. On the other hand, as detailed in Section 5.1, $\sqrt{\frac{\mathcal{D}_b}{\mathcal{M}}}$ typically amounts to a few nm. Data available in the literature do however not allow to ascertain whether the activation energy for $\mathcal{M}$ is, in general, closer to the activation energy for either δD_b or D_l (Akiva et al., 2014; Dillon and Harmer, 2006; Huang and Humphreys, 1999; Riedel and Blug, 2001; Schmidt and Kraft, 2010; Wonisch et al., 2007). Accounting for the uncertainty about the temperature dependence of the characteristic lengths, Figs 17a and 17b present on two different log-log graphs the dependence on *B* of the dissipations $\dot{Q}_b = \dot{Q}_b^T + \dot{Q}_b^\kappa$ and $\dot{Q}_l = \dot{Q}_l^T + \dot{Q}_l^\kappa$ according to Eqs. (57), (58) with q_l = 1.6 (Eqs. (88), (90), and (91)). Whereas the units for $\dot{Q}$ are $\frac{B^2\dot{\theta}^2}{\mathcal{D}_l}$ in both cases, the units for *B* are $\sqrt{\frac{\mathcal{D}_b}{\mathcal{M}}}$ in Fig. 17a and $\frac{\mathcal{D}_l}{\mathcal{M}}$ in Fig. 17b. For $\frac{\delta D_b}{D_l}$, three values are considered which are defined as $\frac{\delta D_b}{D_l} = \delta_b\sqrt{\frac{\mathcal{D}_b}{\mathcal{M}}}$ in Fig. 17a and as $\frac{\delta D_b}{D_l} = \delta_l \frac{\mathcal{D}_l}{\mathcal{M}}$ in Fig. 17b, with δ_b or δ_l = 10, 100, and 1000. An increase of δ_b or δ_l represents in both graphs the effect of a decrease of temperature without change of grain size. For $\dot{Q}_l$ only the curve for δ_b or δ_l = 10 is represented because the curves become (slightly)

different only at very low *B*. For $\dot{Q}_b$, two curves are drawn using either Eq. (88) or Eq. (90): the departure between these curves attests for the difference between the two equations. The dashed black line represents $\dot{Q}_l^T$ expressed by Eq. (58) with q_l = 1.6 (Moldovan et al., 2001) whereas the dashed red lines represents $\dot{Q}_b^T$ according to Eq. (57). The crossing of the curves $\dot{Q}_l$ and $\dot{Q}_b$ corresponds to the *B* value at the transition between the two diffusion modes.

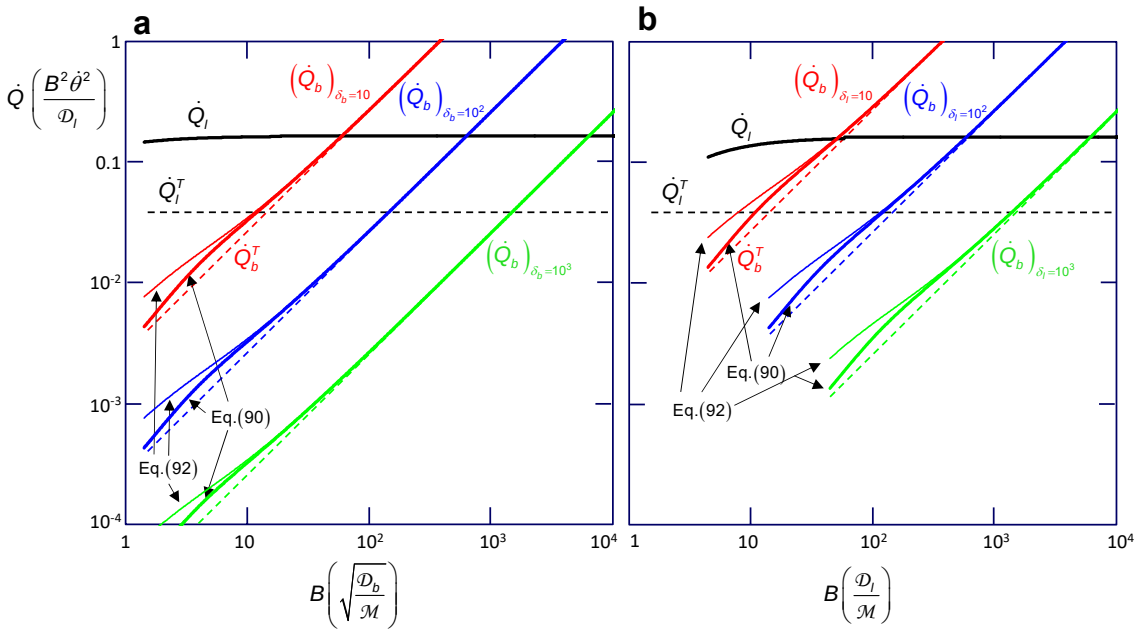

Figure 17: Dependence on length scale *B* of total dissipations $\dot{Q}_l = \dot{Q}_l^T + \dot{Q}_l^\kappa$ for δ_b or δ_l = 10 and $\dot{Q}_b = \dot{Q}_b^T + \dot{Q}_b^\kappa$ for δ_b or δ_l = 10, 100, and 1000. (a) The units for *B* are $\sqrt{\frac{\mathcal{D}_b}{\mathcal{M}}}$ and $\delta_b = \frac{\delta D_b}{D_l}\sqrt{\frac{\mathcal{M}}{\mathcal{D}_b}}$. (b) The units for *B* are $\frac{\mathcal{D}_l}{\mathcal{M}}$ and $\delta_l = \frac{\delta D_b}{D_l}\frac{\mathcal{M}}{\mathcal{D}_l}$.

As $\dot{Q}_b^T$ varies as B^3, the dependence on *B* of the ratio of the dissipation due to κ and to T_n tends to

$$\frac{\dot{Q}_b^{\kappa}+\dot{Q}_l^{mig}}{\dot{Q}_b^{T}} \cong \frac{5}{\sqrt{2}}\frac{1}{B}\sqrt{\frac{\mathcal{D}_b}{\mathcal{M}}}\,, \tag{94}$$

This is reflected in Fig. 17 by the fact that the curves $\dot{Q}_b$ tend asymptotically towards the straight lines $\dot{Q}_b^T$ when *B* increases: in the case of GB-layer diffusion, the dissipation contribution arising from GB curvature becomes significant with respect to $\dot{Q}_b^T$ only at very small grain size. In contrast, as $\dot{Q}_l^{\kappa}$, $\dot{Q}_l^{mig}$, and $\dot{Q}_l^T$ all vary as B^2, the curve $\dot{Q}_l$ shows little dependence on *B* in Fig. 17. The difference between the curve $\dot{Q}_l$ and the horizontal line $\dot{Q}_l^T$ represents the ratio of the dissipations due to κ and to T_n, which tends in that case to

$$\frac{\dot{Q}_l^{\kappa}+\dot{Q}_l^{mig}}{\dot{Q}_l^{T}} \cong \frac{1}{q_l}\frac{15}{\pi} \tag{95}$$

If $q_l \cong 1.6$ (as reported by Moldovan et al (Moldovan et al., 2001)), the ratio is about 3. Hence, in the case of bulk diffusion, GB curvature brings, whatever the grain size, an increase by a factor 4 of the dissipation with respect to the dissipation due solely to normal tractions T_n. The critical grain size up to which GB-layer diffusion is predicted to prevail increases by the same factor. In the case of bulk diffusion, the larger dissipation arising from the presence of GB curvature can be qualitatively justified by referring to the **J** field drawn in Fig. 16: the fact that fluxes do not transfer across outgoing GBs strongly affects the **J** field, which is likely to yield a significantly larger dissipation than predicted via the classical model.

Via Eq. (92), the dissipations contributions $\dot{Q}^{\kappa}$ and $\dot{Q}^{mig}$ arising from GB curvature may be translated into an apparent GB-viscosity

$$\eta = \frac{1}{2\sqrt{3}}\frac{\dot{Q}^{\kappa}+\dot{Q}^{mig}}{B\dot{\theta}^2} \tag{96}$$

In the case of GB-layer diffusion, Eq. (96) yields a non-dimensional GB-viscosity

$$\tilde{\eta}_b \cong 0.011\, m_b \tag{97}$$

The latter is lower by a factor 20 than the result obtained in Eq. (47) for the case of affine deformation. This illustrates the fact that the apparent GB-viscosity ascribed to curvature is not a material property but depends very much on the loading configuration. As shown in the Appendix, if all grains forming the hexagonal lattice rotate simultaneously with the same angular velocity, $\dot{Q}^T = \dot{Q}^\kappa = 0$, $\dot{Q}^{mig}$ is linear with *B*, and the apparent GB-viscosity is simply $\eta = \frac{1}{9}\frac{1}{\mathcal{M}}$.

5. Discussion

5.1. Comparison with data for GB mobility, GB diffusivity, and apparent GB-viscosity

According to the analyses presented in Sections 3 and 4, the role of $\mathcal{M}$ in diffusional deformation emerges via the length scales $\sqrt{\frac{\mathcal{D}_b}{\mathcal{M}}}$ and $\frac{\mathcal{D}_l}{\mathcal{M}}$. Gottstein and co-workers have documented the fact that, even though the activation energies may be similar, mobility, $\mathcal{M}$, and diffusivities, δD_b and D_l, are unrelated material properties because they involve distinct mechanisms (Gottstein and Shvindlerman, 2009; Rollett et al., 2004; Winning et al., 2002; Winning et al., 2010). In spite of the wealth of work based on simulations by molecular dynamics, theoretical estimates of the dependence of $\mathcal{M}$ on the crystallography of the GB remain little validated. We can thus rely only on experimental data derived from grain growth rate measurements. Such experiments have demonstrated that, with respect to pure polycrystals, $\mathcal{M}$ can be strongly reduced in solid solutions and alloys owing to solute-drag,

precipitate-drag, or pore-drag effects (Gottstein and Shvindlerman, 2009; Powers and Glaeser, 1998). From Eqs. (2) and (47), the lower bound for the value to be ascribed to the apparent GB-viscosity in continuum models for the simulation of creep, sintering, or Earth's mantle rheology translates into

$$(\eta)_{lb} = \frac{R_G^2}{\mathcal{D}_b}(\tilde{\eta}_b)_{lb} = 0.29\, R_G \sqrt{\frac{1}{\mathcal{D}_b \mathcal{M}}}\,. \tag{98}$$

$(\eta)_{lb}$ scales as R_G whereas $(\tilde{\eta}_b)_{lb}$ scales as R_G^{-1}. $(\eta)_{lb}$ would be the actual value of η if the intrinsic GB-viscosity may be neglected. Eq. (98) suggests that it should be possible to increase η with respect to its value in pure polycrystals by tuning the alloy composition in such a way as to decrease $\mathcal{M}$ via the solute-drag or precipitate-drag effect (assuming that δD_b is less affected (Herzig and Mishin, 2005)). This GB strengthening effect would add to the diffusional contribution that can arise from GB serration caused by the presence of GB precipitates (Raj and Ashby, 1971).

Table 1. Data for Al, α-Fe, and Al_2O_3

	$T\,(K)$	$\mathcal{M}\left(skg^{-1}m^2\right)$	[ref.]	$\delta D_b\left(m^3s^{-1}\right)$	[ref.]	$\mathcal{D}_b\left(m^4skg^{-1}\right)$	$\sqrt{\frac{\mathcal{D}_b}{\mathcal{M}}}\,(nm)$
Al	823	7×10^{-11}	(Winning et al., 2010)	2.5×10^{-19}	(Brown and Ashby 1980; Gust et al., 1985)	3.5×10^{-28}	2
	560	3×10^{-13}	(Winning et al., 2010)	2.5×10^{-21}	(Brown and Ashby 1980; Gust et al., 1985)]	3×10^{-30}	3
***α*-Fe**	1073	5×10^{-14}	(Zhang et al., 2020)	1×10^{-17} 1×10^{-19}	(Inoue et al., 2007	8×10^{-27} 8×10^{-29}	400 40

Al_2O_3	1423	5×10^{-18}	(Wonisch et al. 2007)	5×10^{-26} 3.5×10^{-27}	(Wonisch et al., 2007) (Li et al., 2010)	2×10^{-35} 1.5×10^{-36}	2 0.5

Experimentally validated data for $\mathcal{M}$, δD_b and D_l for a given material at a given temperature are scarce in the literature. Table 1 presents data for $\mathcal{M}$ and δD_b retrieved for three typical "pure" polycrystals: aluminium, α-iron, and alumina, together with the corresponding values for the length scale $\sqrt{\frac{\mathcal{D}_b}{\mathcal{M}}}$.

- For aluminium at 823 K and 560 K, the $\mathcal{M}$ values are derived from the Arrhenius law experimentally measured by Winning et al (Winning et al., 2010) whereas the δD_b values are the average ensuing from the empirical correlations proposed by Brown and Ashby (Brown and Ashby, 1980) and Gust et al. (Gust et al., 1985). The weak dependence of $\sqrt{\frac{\mathcal{D}_b}{\mathcal{M}}}$ on T follows from the similarity of the activation energies.
- For α-iron at 1073 K, $\mathcal{M}$ is derived, assuming $\gamma = 1 Jm^{-2}$, from the average of the data points for the product $\gamma\mathcal{M}$ measured by Zhang et al (Zhang et al., 2020) using a method coupling phase-field modelling with x-ray diffraction contrast tomography (the work revealed no correlation between $\gamma\mathcal{M}$ and the five parameters characterizing GBs). The δD_b values are borrowed from the measurements by Inoue et al (Inoue et al., 2007): two different values are mentioned because the authors show that their values for δD_b are two-orders of magnitude larger than previous experimental data in the literature, a difference that they attribute to a probable effect of impurities in former work. The ensuing $\sqrt{\frac{\mathcal{D}_b}{\mathcal{M}}}$ values thus differ by a factor of 10.

- For alumina at 1423 K, $\mathcal{M}$ is the value used by Wonisch et al (Wonisch et al., 2007) in a simulation by the discrete element method of experimental curves for the isothermal sinter-forging of an alumina green with average grain size R_G = 75 nm. For δD_b, two values are given, both based on the activation energy proposed by Ruano et al (Ruano et al., 2003): either the value used by Wonisch et al (Wonisch et al., 2007), or the value used by Li et al (Li et al., 2010) in a simulation via an anisotropic constitutive model of the same experimental curves for Al_2O_3 with R_G = 75 nm as in ref (Guillon et al., 2007; Wonisch et al., 2007).

According to Table 1, $\sqrt{\frac{\mathcal{D}_b}{\mathcal{M}}}$ may vary between 0.5 nm and 400 nm. The larger value for α-Fe at 1073 K may be related to the larger diffusivity in a bcc lattice than in a fcc lattice. Although the available data are limited, Table 1 justifies the choice made in Sections 3 and 4 to consider m_b values in the range $0 \le m_b \le 0.5$ (Eq. (35)). In particular, for Al_2O_3 at 1423 K with R_G = 75 nm, $m_b = 3.5 \times 10^{-2}$ according to the data for δD_b used by Wonisch et al whereas $m_b = 0.9 \times 10^{-2}$ according to the data used by Li et al.

In the case of Al_2O_3 at 1423 K with R_G = 75 nm, the validity of Eqs. (47) and (98) can be evaluated by reference to the papers of Wonisch et al (Wonisch et al., 2007) and Li et al (Li et al., 2010) in which optimum values for η or $\tilde{\eta}$ in simulation codes were identified via a reverse procedure:

- the optimum for η identified by Wonisch et al was $\eta = 6 \times 10^{18}$ kg.s^{-1}.m^{-2}; in comparison, with R_G = 75 nm, the data for $\mathcal{M}$ and $\mathcal{D}_b$ in Table 1 yield via Eq. (98) $(\eta)_{lb} = 2 \times 10^{18}$ kg.s^{-1}.m^{-2}.

- the optimum for $\tilde{\eta}_b$ identified by Li et al was $\tilde{\eta}_b = 5 \times 10^{-3}$; in comparison, the data in Table 1 with R_G = 75 nm yield, via Eq. (47), $(\tilde{\eta}_b)_{lb} = 2 \times 10^{-3}$.

Considering the uncertainty on the accuracy of data retrieved from the literature for $\mathcal{M}$ and $\mathcal{D}_b$, the consistency between the present work and these previous results is conspicuous.

5.2. Possibility of observation of GB curvature at grain scale

The GB curvature coupled to GB sliding is a dynamic, out-of-equilibrium phenomenon which vanishes while capillary equilibrium at rest restores after unloading. Direct observation is likely to be very difficult for at least two reasons: (i) it would imply the possibility of high-resolution microstructural observation during straining, and (ii) the strain-rate-induced curvature adds to the curvature that intrinsically exists in a static polycrystal with anisotropic interface properties and random grain shapes. Moreover, the strain-rate-induced curvature would be hard to notice because it concentrates close to TJs. Nevertheless, for the GBs submitted to a traction having both a shear component and a positive normal component, the occurrence of curvature during straining can, in principle, be attested after unloading by a dissymmetrical distribution of the layer of mass deposition between the two sides of the relaxed GB profile (confer the blue lines in Fig. 7c). Experimentally, mass deposition along GBs under tension has commonly been invoked to justify the observation by electron microscopy of dispersoid-free layers (Burton and Reynolds, 1995; McNee et al., 2002) and surface striation layers (Masuda et al., 2019; Rust and Todd, 2011) in metallographic sections of specimens having undergone diffusional creep or superplastic deformation. A recent example is the study by Masuda et al (Masuda et al., 2019) of the GB microstructure evolution during superplastic deformation at 900 °C of an oxide dispersion strengthened ferritic steel with columnar grains: scanning electron microscopy coupled to backscatter electron diffraction reveals frequent asymmetry in the mass deposition

layers along GBs under tension (see Figs. 3 to 6 in the reference). The authors interpret this asymmetry as due to diffusional transfers from convex to concave sides of GBs, driven by the reduction of the grain boundary energy. The present work suggests that the GB curvature gradients that drive these transfers did not pre-exist before deformation but were dynamically generated during the deformation process.

6. Conclusion

Proper account of the dependence of the diffusion potential on both the normal component of the traction vector on grain boundaries and the curvature of grain boundaries provides a novel insight into the interactions between the different types of grain boundary motion during diffusional deformation. Grain boundary curvature being a condition for the transfer of diffusion fluxes across grain boundaries, grain boundary migration and grain boundary mobility are necessary ingredients in the diffusional deformation model. The main outcomes of the analysis can be summarized as follows.

- A link is established between the distribution of curvature and the magnitude of the diffusion fluxes to be transferred across grain boundaries. This link constitutes a boundary condition for the solution of the equation expressing the balance of the different types of grain boundary motion during steady-state or quasi-steady-state deformation.
- The solution of this equation is developed in 2D for the affine deformation of a polycrystal and for the rotation of a grain embedded in a polycrystal. The analysis provides expressions for the dependence, on grain boundary mobility, of (i) the strain-rate-induced curvature, (ii)

the grain boundary profiles, (iii) the diffusion fluxes, and (iv) the contributions to energy dissipation.

- In the case of the rotation of a grain, the conditions of dominance of GB-layer diffusion and dominance of bulk diffusion are compared via an approximate solution of the Laplace equation.
- The contribution of grain boundary curvature to the dissipation reveals to scale nearly as the square of grain size. It follows that the relative influence of grain boundary curvature is larger in conditions of Nabarro-Herring creep than in conditions of Coble creep.
- In the case of Coble creep, the contribution of grain boundary curvature to dissipation may be translated into a lower bound for the apparent grain boundary viscosity parameter to be used in numerical simulations. This lower bound is consistent with previous identifications of the parameter in the literature.
- The classical model assuming flat grain boundaries emerges as a particular case involving the implicit assumption of an infinite grain boundary mobility.

Appendix: simultaneous rotation of the grains

In the hypothetical case where all grains in a regular lattice of hexagonal grains would rotate simultaneously with the same angular velocity $\dot{\theta}$, $\Delta\dot{u}_{sl} = -2H\dot{\theta}$ and $\Delta\dot{u}_n = 0$ (this is not true if grains are not equiaxed or if adjacent grain sizes are different). Eq. (59) then reduces to

$$\dot{u}_n^{mig} = -\mathcal{M}\gamma\kappa = x\dot{\theta} \tag{99}$$

Such a hypothetical phenomenon would thus involve no diffusion fluxes. GB curvature is then linked only to the migration bringing the steady-state rotation of the GBs with respect to grain

lattices. Instead of Eq. (85), the solution of the problem yields $z = \frac{1}{6}\left(-\frac{x}{B}+\frac{x^3}{B^3}\right)\frac{B^3\dot{\theta}}{\gamma\mathcal{M}}$ with $(\varphi)_{x=\pm B} = \frac{1}{3}\frac{B^2\dot{\theta}}{\gamma\mathcal{M}}$, which means a rotation of the steady-state orientation of the tangents the GBs meeting at TJs in the same direction as $\dot{\theta}$. The dissipation rate per unit volume then arises solely from GB migration and GB sliding. One obtains via Eqs. (99) and (91), $\dot{Q}^{mig} = \frac{2}{3\sqrt{3}}\frac{B\dot{\theta}^2}{\mathcal{M}}$. $\dot{Q}^{mig}$ thus varies linearly with *B* and, according to Eq.(96), the apparent GB-viscosity would write simply $\eta^{\kappa} = \frac{1}{9}\frac{1}{\mathcal{M}}$.

Acknowledgements

The author is indebted to Prof Laurence Brassart (University of Oxford, UK) for her comments on preliminary versions of the manuscript. This research did not receive any specific grant from funding agencies in the public, commercial, or not-for-profit sectors.

References

Akiva, R., Katsman, A., Kaplan, W.D., 2014. Anisotropic grain boundary mobility in undoped and doped alumina. Journal of the American Ceramic Society 97, 1610-1618.

Ashby, M., 1972. Boundary defects, and atomistic aspects of boundary sliding and diffusional creep. Surface Science 31, 498-542.

Ashby, M.F., 1969. On interface-reaction control of Nabarro-Herring creep and sintering. Scripta Metallurgica 3, 837-842.

Ashby, M.F., Raj, R., Gifkins, R.C., 1970. Diffusion-controlled sliding at a serrated grain boundary. Scripta Metallurgica 4, 737-741.

Balluffi, R.W., 1982. Grain boundary diffusion mechanisms in metals. Metallurgical Transactions A 13, 2069-2095.

Balluffi, R.W., Allen, S., Carter, W.C., 2005. Kinetics of materials. John Wiley & Sons.

Beere, W., 1976. Stress redistribution during Nabarro-Herring and superplastic creep. Metal Science 10, 133-139.

Beere, W., 1977. Grain-boundary sliding controlled creep: its relevance to grain rolling and superplasticity. Journal of Materials Science 12, 2093-2098.

Beere, W., 1978. Stresses and Deformation at Grain Boundaries [and Discussion]. Philosophical Transactions of the Royal Society of London A: Mathematical, Physical and Engineering Sciences 288, 177-196.

Bell, R., Langdon, T., 1967. An investigation of grain-boundary sliding during creep. Journal of Materials Science 2, 313-323.

Bower, A.F., Wininger, E., 2004. A two-dimensional finite element method for simulating the constitutive response and microstructure of polycrystals during high temperature plastic deformation. Journal of the Mechanics and Physics of Solids 52, 1289-1317.

Brassart, L., Delannay, F., 2019. Bounds for shear viscosity in Nabarro–Herring–Coble creep. Mech Mater 137, 103106.

Brown, A., Ashby, M., 1980. Correlations for diffusion constants. Acta Metallurgica 28, 1085-1101.

Burton, B., 2002. Diffusional rotation of crystals about a common interface. Philosophical Magazine A 82, 51-64.

Burton, B., Greenwood, G., 1985. Analysis of Coble creep in cylindrical and cubic crystals. Mater. Sci. Technol. 1, 1029-1032.

Burton, B., Reynolds, G.L., 1995. In defense of diffusional creep. Materials Science and Engineering: A 191, 135-141.

Cahn, J.W., Mishin, Y., Suzuki, A., 2006. Coupling grain boundary motion to shear deformation. Acta Materialia 54, 4953-4975.

Cahn, J.W., Taylor, J.E., 1994. Overview no. 113 surface motion by surface diffusion. Acta metallurgica et materialia 42, 1045-1063.

Cahn, J.W., Taylor, J.E., 2004. A unified approach to motion of grain boundaries, relative tangential translation along grain boundaries, and grain rotation. Acta Materialia 52, 4887-4898.

Cannon, W.R., 1972. The contribution of grain boundary sliding to axial strain during diffusion creep. Philosophical Magazine 25, 1489-1497.

Cannon, W.R., Sherby, O.D., 1977. Creep Behavior and Grain-Boundary Sliding in Polycrystalline A12O3. Journal of the American Ceramic Society 60, 44-47.

Ch'ng, H.N., Pan, J., 2004. Cubic spline elements for modelling microstructural evolution of materials controlled by solid-state diffusion and grain-boundary migration. Journal of Computational Physics 196, 724-750.

Coble, R., 1963. A model for boundary diffusion controlled creep in polycrystalline materials. J Appl Phys 34, 1679-1682.

Cocks, A., 1996. Variational principles, numerical schemes and bounding theorems for deformation by Nabarro-Herring creep. Journal of the Mechanics and Physics of Solids 44, 1429-1452.

Cocks, A.C.F., 1994. Overview no. 117 The structure of constitutive laws for the sintering of fine grained materials. Acta Metallurgica et Materialia 42, 2191-2210.

Delannay, F., Brassart, L., 2018. Transient and asymptotic kinetics of mass transfer by coupled surface and grain boundary diffusion in sintering under strain rate control. Proceedings of the Royal Society A: Mathematical, Physical and Engineering Science 474.

Delannay, F., Brassart, L., 2020. Variational analysis of the influence of grain shape anisotropy on shear viscosity in Nabarro-Herring-Coble creep. Mech Mater 143, 103312.

Delannay, F., Missiaen, J.M., 2009. Experimental validation of a new model for the initial stage of sintering of single phase systems. Acta Materialia 57, 420-431.

Dillon, S.J., Harmer, M.P., 2006. Intrinsic grain boundary mobility in alumina. Journal of the American Ceramic Society 89, 3885-3887.

Fisher, J.C., 1951. Calculation of Diffusion Penetration Curves for Surface and Grain Boundary Diffusion. J Appl Phys 22, 74-77.

Ford, J., Wheeler, J., Movchan, A., 2002. Computer simulation of grain-boundary diffusion creep. Acta Materialia 50, 3941-3955.

Fukutomi, H., Yamamoto, T., Nonomura, K., Takada, K., 1999. Examination of dislocation mechanism on grain boundary sliding in high angle grain boundaries by stress change test. Interface Science 7, 141-146.

Geckinli, A.E., Barrett, C.R., 1976. Superplastic deformation of the Pb-Sn eutectic. Journal of Materials Science 11, 510-521.

Gibbs, G., 1965. Fluage par diffusion dans les solides polycristallins. Memoires Scientifiques De La Revue De Metallurgie 62, 781-&.

Gibbs, G., 1968. The role of grain-boundary sliding in high-temperature creep. Materials Science and Engineering 2, 269-272.

Gifkins, R.C., Langdon, T.G., 1970. Grain boundary displacements due to diffusional creep. Scripta Metallurgica 4, 563-566.

Gottstein, G., Shvindlerman, L.S., 2009. Grain boundary migration in metals: thermodynamics, kinetics, applications. CRC press.

Greenwood, G.W., 1985. An analysis of the effect of multiaxial stresses and grain shape on Nabarro-Herring creep. Philosophical Magazine A 51, 537-542.

Greenwood, G.W., 1992. A formulation for anisotropy in diffusional creep. Proc. R. Soc. Lond. A 436, 187-196.

Guillon, O., Aulbach, E., Rödel, J., Bordia, R.K., 2007. Constrained Sintering of Alumina Thin Films: Comparison Between Experiment and Modeling. Journal of the American Ceramic Society 90, 1733-1737.

Gust, W., Mayer, S., Bögel, A., Predel, B., 1985. Generalized representation of grain boundary self-diffusion data. Le Journal de Physique Colloques 46, C4-537-C534-544.

Han, J., Thomas, S.L., Srolovitz, D.J., 2018. Grain-boundary kinetics: A unified approach. Progress in Materials Science 98, 386-476.

Harris, K., Singh, V., King, A., 1998. Grain rotation in thin films of gold. Acta materialia 46, 2623-2633.

Hazzledine, P., Schneibel, J., 1993. Theory of Coble creep for irregular grain structures. Acta metallurgica et materialia 41, 1253-1262.

Henrich, B., Wonisch, A., Kraft, T., Moseler, M., Riedel, H., 2007. Simulations of the influence of rearrangement during sintering. Acta Materialia 55, 753-762.

Herring, C., 1950. Diffusional Viscosity of a Polycrystalline Solid. J Appl Phys 21, 437-445.

Herring, C., 1953. The use of classical macroscopic concepts in surface energy problems, in: Gomer, R., Smith, C.S. (Eds.), Structure and properties of solid surfaces. the University of Chicago Press, Lake Geneva, Wisconsin, USA, p. 5.

Herzig, C., Mishin, Y., 2005. Grain boundary diffusion in metals, Diffusion in Condensed Matter. Springer, pp. 337-366.

Hirth, J.P., 1994. Dislocations, steps and disconnections at interfaces. Journal of Physics and Chemistry of Solids 55, 985-989.

Hirth, J.P., Pond, R.C., 1996. Steps, dislocations and disconnections as interface defects relating to structure and phase transformations. Acta Materialia 44, 4749-4763.

Hirth, J.P., Wang, J., Tomé, C.N., 2016. Disconnections and other defects associated with twin interfaces. Progress in Materials Science 83, 417-471.

Hotz, W., Ruedl, E., Schiller, P., 1975. Observation of processes of superplasticity with the scanning electron microscope. Journal of Materials Science 10, 2003-2006.

Huang, Y., Humphreys, F.J., 1999. Measurements of grain boundary mobility during recrystallization of a single-phase aluminium alloy. Acta Materialia 47, 2259-2268.

Inoue, A., Nitta, H., Iijima, Y., 2007. Grain boundary self-diffusion in high purity iron. Acta Materialia 55, 5910-5916.

Kashyap, B.P., Arieli, A., Mukherjee, A.K., 1985. Microstructural aspects of superplasticity. Journal of Materials Science 20, 2661-2686.

Kim, B.-N., Hiraga, K., Morita, K., 2005. Viscous grain-boundary sliding and grain rotation accommodated by grain-boundary diffusion. Acta materialia 53, 1791-1798.

Kim, B.-N., Hiraga, K., Morita, K., Ahn, B.-W., 2004. Analysis of creep due to grain-boundary diffusion in hexagonal microstructures. Philosophical Magazine 84, 3251-3262.

Kim, B.-N., Hiraga, K., Morita, K., Yoshida, H., Ahn, B.-W., 2009. Viscous grain-boundary sliding with rotating particles or grains. Acta Materialia 57, 5730-5738.

Kim, H.S., Estrin, Y., Bush, M.B., 2000. Plastic deformation behaviour of fine-grained materials. Acta Materialia 48, 493-504.

Langdon, T.G., 1981. Observations on the magnitude of grain boundary sliding in Region 1 of superplasticity. Journal of Materials Science 16, 2613-2616.

Li, F., Pan, J., Guillon, O., Cocks, A., 2010. Predicting sintering deformation of ceramic film constrained by rigid substrate using anisotropic constitutive law. Acta Materialia 58, 5980-5988.

Lifshitz, I., 1963. On the theory of diffusion-viscous flow of polycrystalline bodies. Soviet Physics JETP 17, 909-920.

Linne, M.A., Venkataraman, A., Sangid, M.D., Daly, S., 2019. Grain Boundary Sliding and Slip Transmission in High Purity Aluminum. Experimental Mechanics 59, 643-658.

Liu, F.C., Ma, Z.Y., 2010. Contribution of grain boundary sliding in low-temperature superplasticity of ultrafine-grained aluminum alloys. Scripta Materialia 62, 125-128.

Masuda, H., Sato, E., 2020. Diffusional and dislocation accommodation mechanisms in superplastic materials. Acta Materialia 197, 235-252.

Masuda, H., Tobe, H., Sato, E., Sugino, Y., Ukai, S., 2019. Diffusional mass flux accommodating two-dimensional grain boundary sliding in ODS ferritic steel. Acta Materialia 176, 63-72.

McNee, K., Greenwood, G., Jones, H., 2001. Microstructural evidence for diffusional creep in copper using atomic force microscopy. Scripta materialia 44, 351-357.

McNee, K.R., Greenwood, G.W., Jones, H., 2002. Observation and interpretation of some microstructural features of low stress creep. Scripta Materialia 47, 619-623.

Moldovan, D., Wolf, D., Phillpot, S.R., 2001. Theory of diffusion-accommodated grain rotation in columnar polycrystalline microstructures. Acta Materialia 49, 3521-3532.

Mori, T., Nakasone, Y., Taya, M., Wakashima, K., 1997. Steady-state creep rate of a composite: Two-dimensional analysis. Philosophical Magazine Letters 75, 359-365.

Mori, T., Onaka, S., Wakashima, K., 1998a. Role of grain-boundary sliding in diffusional creep of polycrystals. J Appl Phys 83, 7547-7552.

Mori, T., Taya, M., Wakashima, K., 1998b. Steady-state creep of a composite analysed by an energy balance method. Philosophical Magazine Letters 78, 331-338.

Nabarro, F.R.N., 1948. Deformation of crystals by the motion of single ions, Conference on Strength of Solids. Physical Society London, Bristol, pp. 75-90.

Onaka, S., Madgwick, A., Mori, T., 2001. Kinetics of diffusional creep discussed by energy dissipation and effect of grain-size distribution on the rate equations. Acta Materialia 49, 2161-2168.

Pan, J., Cocks, A., Kucherenko, S., 1997. Finite element formulation of coupled grain-boundary and surface diffusion with grain-boundary migration. Proceedings of the Royal Society of London. Series A: Mathematical, Physical and Engineering Sciences 453, 2161-2184.

Pan, J., Cocks, A.C.F., 1993. Computer simulation of superplastic deformation. Comput Mater Sci 1, 95-109.

Powers, J.D., Glaeser, A.M., 1998. Grain boundary migration in ceramics. Interface Science 6, 23-39.

Rachinger, W.A., 1952. Relative grain translations in the plastic flow of aluminium. J. Inst. Metals 81, 33.

Raj, R., Ashby, M.F., 1971. On grain boundary sliding and diffusional creep. Metallurgical transactions 2, 1113-1127.

Reynolds, G., Burton, B., Speight, M., 1975. Creep fracture processes in uranium dioxide. Acta Metallurgica 23, 573-577.

Riedel, H., Blug, B., 2001. A comprehensive model for solid state sintering and application to silicon carbide, in: Chuang, T.-J., Rudnicki, J. (Eds.), James R. Rice 60th Anniversary Kluwer Academic Publishers, Dordrecht Boston London, pp. 49-70.

Riedel, H., Svoboda, J., 1993. A theoretical study of grain growth in porous solids during sintering. Acta metallurgica et materialia 41, 1929-1936.

Riedel, H., Zipse, H., Svoboda, J., 1994. Equilibrium pore surfaces, sintering stresses and constitutive equations for the intermediate and late stages of sintering—II. Diffusional densification and creep. Acta metallurgica et materialia 42, 445-452.

Rollett, A.D., Gottstein, G., Shvindlerman, L.S., Molodov, D.A., 2004. Grain boundary mobility - A brief review. Zeitschrift fuer Metallkunde/Materials Research and Advanced Techniques 95, 226-229.

Ruano, O.A., Wadsworth, J., Sherby, O.D., 2003. Deformation of fine-grained alumina by grain boundary sliding accommodated by slip. Acta Materialia 51, 3617-3634.

Rudge, J.F., 2018. The Viscosities of Partially Molten Materials Undergoing Diffusion Creep. Journal of Geophysical Research: Solid Earth 123, 10,534-510,562.

Rust, M.A., Todd, R.I., 2011. Surface studies of Region II superplasticity of AA5083 in shear: Confirmation of diffusion creep, grain neighbour switching and absence of dislocation activity. Acta Materialia 59, 5159-5170.

Schmidt, I., Kraft, T., 2010. Simulation of the co-sintering of composite structures. Int. J. Mater. Res. 101, 933-941.

Shah, S., Chokshi, A.H., 1998. The significance of diffusional flow in ultrafine-grained materials. Colloids and Surfaces A: Physicochemical and Engineering Aspects 133, 57-61.

Spingarn, J., Nix, W., 1978. Diffusional creep and diffusionally accommodated grain rearrangement. Acta Metallurgica 26, 1389-1398.

Svoboda, J., Riedel, H., 1995a. New solutions describing the formation of interparticle necks in solid-state sintering. Acta metallurgica et materialia 43, 1-10.

Svoboda, J., Riedel, H., 1995b. Quasi-equilibrium sintering for coupled grain-boundary and surface diffusion. Acta metallurgica et materialia 43, 499-506.

Thorsen, P., Bilde-Sørensen, J., 1999. Deposition of material at grain boundaries in tension interpreted in terms of diffusional creep. Materials Science and Engineering: A 265, 140-145.

Venkataraman, A., Linne, M., Daly, S., Sangid, M.D., 2019. Criteria for the prevalence of grain boundary sliding as a deformation mechanism. Materialia 8, 100499.

Wakai, F., Brakke, K.A., 2011. Mechanics of sintering for coupled grain boundary and surface diffusion. Acta Materialia 59, 5379-5387.

Wakai, F., Nikolić, Z.S., 2011. Effect of grain boundary sliding on shear viscosity and viscous Poisson's ratio in macroscopic shrinkage during sintering. Acta Materialia 59, 774-784.

Wei, Y., Bower, A.F., Gao, H., 2008. Recoverable creep deformation and transient local stress concentration due to heterogeneous grain-boundary diffusion and sliding in polycrystalline solids. Journal of the Mechanics and Physics of Solids 56, 1460-1483.

Wheeler, J., 2010. Anisotropic rheology during grain boundary diffusion creep and its relation to grain rotation, grain boundary sliding and superplasticity. Philosophical Magazine 90, 2841-2864.

Winning, M., Gottstein, G., Shvindlerman, L.S., 2002. On the mechanisms of grain boundary migration. Acta Materialia 50, 353-363.

Winning, M., Rollett, A.D., Gottstein, G., Srolovitz, D.J., Lim, A., Shvindlerman, L.S., 2010. Mobility of low-angle grain boundaries in pure metals. Philosophical Magazine 90, 3107-3128.

Wonisch, A., Guillon, O., Kraft, T., Moseler, M., Riedel, H., Rödel, J., 2007. Stress-induced anisotropy of sintering alumina: Discrete element modelling and experiments. Acta Materialia 55, 5187-5199.

Zhang, J., Ludwig, W., Zhang, Y., Sørensen, H.H.B., Rowenhorst, D.J., Yamanaka, A., Voorhees, P.W., Poulsen, H.F., 2020. Grain boundary mobilities in polycrystals. Acta Materialia 191, 211-220.